Westfälische Wilhelms-Universität Münster

Institut für Kernphysik
September 2016

Masterarbeit

Optimierung der Auflösung einer Kleintier-PET-Kamera

Optimization of the Resolution of a Small-Animal-PET-Camera

Vorgelegt von Jens Robert Lühder

Hiermit versichere ich, dass ich die vorliegende Arbeit selbständig verfasst und keine anderen als die angegebenen Hilfsmittel benutzt habe. Die Stellen der Arbeit, die dem Wortlaut oder dem Sinn nach anderen Werken entnommen sind, wurden unter Angabe der Quelle kenntlich gemacht. Münster, 01.09.2016

Contents

1 Introduction

Modern diagnostic medicine often relies on imaging modalities. There are different imaging modalities like single-photon emission computed tomography (SPECT), computed tomography (CT) or magnetic resonance imaging (MRT) while this work will be about positron emission tomography (PET). PET is a non-invasive in-vivo imaging technique that uses radioactive β^+-emitters. The radionuclides in in-vivo PET are used to label compounds of biological interest [1] which are then injected to a living organism. This radioactive compound is called a tracer. The positron, emitted by the tracer, annihilates with a nearby electron and emits two gamma rays in an angle of approximately 180° (back-to-back). By detecting these photons the spatial distribution of the radioactive density can be calculated. Common PET scanners use scintillation crystal based detectors and have a resolution of 1 mm or worse. The PET scanner used in this work is a High-Density-Avalanche-Chamber (HIDAC) and uses Multi-Wire-Proportional-Chambers (MWPC) as detector modules. It is not possible to distinguish between the energy of incoming gamma-rays with a MWPC, but the possibility to reach better resolution and lower production costs still makes the HIDAC a promising scanner. The resolution of PET systems is limited by two physical effects: The positron range and the non-colinearity. The positron range is the distance that a positron travels through matter until it annihilates and is dependent on its energy and the traversed material. The non-colinearity describes the deviation of the the emission angle of 180°. While the blurring caused by these effects can be considered small in human PET imaging [2], it plays a significant role in small animal PET Scanners as the volume of organs is much smaller in small animals. The resolution of a PET scanner is furthermore limited by the resolution of the detector modules the scanner uses. The spatial resolution of HIDAC modules relies on the measurements of the charge distributions created during an event. Hence it is necessary to gather information about the response function of a detector module to increase the possible resolution of the HIDAC.

2 Theoretical Basics

In the following part, the β^+-decay will be discussed and the interaction of charged particles and photons with matter will be elaborated. After an explanation of the basics of Positron Emission Tomography, the functionality of gas detectors will be shown.

2.1 Decays

In general there are three kinds of decays: α-, β- and γ- decay. Comprehensive literature about the decays can be found in [3]. In the case of PET (Positron Emission Tomography), β^+-decay is the relevant one. In α-decay a helium nucleus $^4\mathrm{He}^{2+}$ is emitted. Compared to other decay processes, α-particles have a relatively high mass and deposit a high amount of energy in small volumes. Hence, they can do severe damage to tissue but can be shielded easily due to their high cross section. In β-decay, so called β-particles are emitted, where an electron is called a β^-- and a positron is called a β^+-particle. In β^+-decay a proton is converted into a neutron due to the weak interaction and a positron (e^+) is emitted, whereas in the β^--decay a neutron is converted into a proton and an electron (e^-) is emitted. The velocity of the emitted β-particles follows a continuous distribution. If only two particles are involved into the process, the observation of continuous spectrum would violate the energy and momentum conservation. Therefore, a new particle was postulated and later discovered. This particle is called neutrino. The β^- decay can be described as:

$$^A_ZX \rightarrow ^A_{Z+1} Y + e^- + \bar{\nu}_e + Q \tag{2.1}$$

And the β^+-decay is given by:

$$^A_ZX \rightarrow ^A_{Z-1} Y + e^+ + \nu_e + Q \tag{2.2}$$

Z is the charge number, A is the mass number, ${}^{A}_{Z}X$ is the mother nucleus, ${}^{A}_{Z+1}Y$ and ${}^{A}_{Z-1}Y$ are the daughter nuclei and Q is the energy gain of the decay. In many cases, the daughter nucleus is left in an excited state, which de-excites through emission of photons (γ-decay). Because the decay produces three daughter-particles, the kinetic energy of the particles is not fixed, but dependent on their emission angle. The neutron is heavier than the proton. Hence, β^{+}-decay is only possible for protons bound in a nucleus whose binding energy difference is sufficient for this process. An additional effect that competes with β^{+}-decay is the electron capture (EC) process:

$$ {}^{A}_{Z}X + e^{-} \rightarrow {}^{A}_{Z-1}Y + \nu_e + Q \tag{2.3} $$

In case of electron capture, an electron of the inner atomic shell is captured to form a neutron [3]. However, the competition of the EC with β-decay is no principle problem for PET, because it is not associated with the production of two coincident photons.

2.2 Interaction of Positrons, Electrons and Photons

Positrons, electrons and photons differ in their behavior when interacting with matter. It is important for the understanding of PET to know which interactions occur and what is their probability to do so.

2.2.1 Charged Particles

Charged particles propagating in matter will undergo an energy loss per distance -$\frac{dE}{dx}$ due to interaction with the coulomb field of atomic electrons. The path length dx is normally given in $\frac{g}{cm^2}$. This is common because $dx = \rho ds$ is largely independent of the material. Here, ds is the transversed distance in the matter and ρ is its density. A detailed discussion of the theory can be found in [4]. The entire energy loss can be described as sum of several energy losses.

$$ -\frac{dE}{dx} = -\frac{dE}{dx}|_{\text{Ion}} - \frac{dE}{dx}|_{\text{Photo}} - \frac{dE}{dx}|_{\text{Brems}} - \frac{dE}{dx}|_{\text{Pair}} \tag{2.4} $$

$-\frac{dE}{dx}|_{\text{Ion}}$ describes the energy loss through ionization and excitation of matter, $-\frac{dE}{dx}|_{\text{Photo}}$ describes the energy loss through inelastic scattering with nuclei, $-\frac{dE}{dx}|_{\text{Brems}}$ describes the energy loss through Bremsstrahlung and $-\frac{dE}{dx}|_{\text{Pair}}$ describes the energy loss through pair production. The ionization loss for charged particles can be described through the Bethe-Bloch formula [5]

$$-\frac{dE}{dx}|_{\text{Ion}} = \frac{4\pi r_e^2 m_e c^2 N_0 Z z^2}{A\beta^2}\left[\ln\left(\frac{2m_e c^2\beta^2\gamma^2}{I}\right) - \beta^2 - \frac{\delta}{2}\right] \tag{2.5}$$

where c is the speed of light, m_e is the electron mass, v is the velocity, $\beta = \frac{v}{c}$, $\gamma = \frac{1}{\sqrt{1-\beta^2}}$, N_0 is the Avogadro constant, Z is the nuclear charge, $r_e = 2.8\,\text{fm}$ is the classic electron radius, A is the mass number of the medium and I is the effective ionization potential. δ is a correction parameter, which corresponds to the density effect: Polarizable atoms are shielding the field of incident particles and reduce the energy loss. As it is dependent on the density of the material, the effect has more influence in dense materials like lead. In gases, the influence is negligible.
It can be seen that $\frac{dE}{dx}$ is independent of the particle mass M but dependent upon the velocity of the particle. At low energies the behavior of the energy loss is described by the first term. With increasing $\beta\gamma$ the value of $\frac{dE}{dx}$ decreases with $\frac{1}{\beta^2}$ as the time the incident particle has to interact with the Coulomb field of the atom decreases. The energy loss reaches a minimum at $\beta\gamma \approx 3$ and then rises again. The relativistic rise due to the extended transverse field for relativistic particles is described by the logarithmic term. The formula is only valid for particles heavier than electrons. For electrons, the incident particle is the same particle as the shell electrons. Because these particles are not distinguishable, the approximation of the energy loss for electrons changes to [4]:

$$\begin{aligned}-\frac{dE}{dx}|_{Ion} = \frac{4\pi r_e^2 m_e c^2 N_0 Z}{A\beta^2}[\ln\left(\frac{\gamma m_e c^2\beta\sqrt{\gamma-1}}{\sqrt{2}I}\right) + \frac{1}{2}\left(1-\beta^2\right)\\ - \frac{2\gamma-1}{2\gamma^2}\ln 2 + \frac{1}{16}\left(\frac{\gamma-1}{\gamma}\right)^2]\end{aligned} \tag{2.6}$$

Considering that positrons are as heavy as electrons but are not the same particles, positrons follow a different distribution [4]:

$$\begin{aligned}-\frac{dE}{dx}|_{Ion} = \frac{4\pi r_e^2 m_e c^2 N_0 Z}{A\beta^2}[\ln\left(\frac{\gamma m_e c^2\beta\sqrt{\gamma-1}}{\sqrt{2}I}\right)\\ - \frac{\beta^2}{24}\left(23 + \frac{14}{\gamma+1} + \frac{10}{(\gamma+1)^2} + \frac{4}{(\gamma+1)^3}\right)]\end{aligned} \tag{2.7}$$

In PET the energy loss due to ionization has the greatest influence on the total energy loss.

Charged particles exchange virtual photons with atomic nuclei which results in an inelastic scattering. The energy loss given by this photo-nuclear interaction is given by [4]:

$$-\frac{dE}{dx}|_{Photo} = b_{\text{Nucleus}}(Z, A, E)^2 E \tag{2.8}$$

The energy loss due to this effect is nearly proportional to the energy. Compared to the energy loss caused by ionization the influence of this effect is low.

If the energy of the incident particle is high, it is also possible to create new particles in the coulomb field of nearby atoms. This effect is called pair production. To create a pair of an electron and a positron, an energy of at least 1022 keV is needed. Pair production generates an energy loss of [4]:

$$-\frac{dE}{dx}|_{Pair} = b_{\text{Pair}}(Z, A, E)^2 E \tag{2.9}$$

For PET pair production is a negligible effect.

In addition to these effects, charged particles with high velocity emit photons in the Coulomb field of nearby atoms. For such particles whith high energies, the energy loss caused by Bremsstrahlung can be calculated as [4]:

$$-\frac{dE}{dx}|_{Brems} = 4\alpha N_0 \frac{Z^2}{A} z^2 \left(\frac{1}{4\pi\epsilon_0}\frac{e^2}{mc^2}\right)^2 E \ln\left(\frac{183}{Z^{\frac{1}{3}}}\right) \tag{2.10}$$

If the incident particle is an electron and $E \gg m_e c^2/\alpha Z^{\frac{1}{3}}$ the equation changes to [4]:

$$-\frac{dE}{dx}|_{Photo} = 4\alpha N_0 \frac{Z^2}{A} r_e^2 E \ln\left(\frac{183}{Z^{\frac{1}{3}}}\right) \tag{2.11}$$

This energy loss is proportional to the energy and anti-proportional to the squared mass of the incident particle. Therefore, Bremsstrahlung has high relevance for electrons and positrons. However, the energy of involved particles in PET is in range of 511 keV or smaller. Due to this fact the influence of Bremsstrahlung in energy loss can be ignored. As mentioned earlier, the total energy loss is dominated by ionization.

2.2.2 Photons

When photons propagate through matter the intensity decreases exponentially. This correlation is described by the Beer-Lambert-Law [6]:

$$I_\nu = I_0 e^{-\mu_\nu x} = I_0 e^{\frac{-\mu_\nu}{\rho}\rho x} \tag{2.12}$$

Where I_0 is the intensity of the incident beam, $\mu_\nu = \rho\sigma_\nu$ is the attenuation coefficient and x is the thickness of the material. ρ is the density of the absorber and σ_ν the cross section for a photon to undergo an interaction process. The quotient $\frac{\mu_\nu}{\rho}$ is called mass attenuation coefficient. There are three different interaction processes a photon can take part in: The Compton effect, the photoelectric effect and the pair production. The photoelectric effect dominates the cross section for small energies of E_γ up to approximately 100 keV. For higher energies at $E_\gamma \approx 1\,\text{MeV}$ the Compton effect has the greatest influence on the cross section. At an energy of 511 keV, the influence of Compton effect and photoelectric effect are of the same magnitude. When the energy of the incident particle is much higher than 1 MeV the cross section of pair production is the most important effect. The mass attenuation coefficient and therefore the cross section dependent on the photon energy can be seen in figure 2.1.

Photoelectric Effect

The photoelectric effect describes a photon which is absorbed by a bound electron, followed by the emission of the electron. The photon is completely absorbed by the electron. Thus the energy of the emitted electron is calculated as the difference between the photon energy and the binding energy of the electron [2]:

$$E_e = h\nu - E_B \tag{2.13}$$

Where h is the Planck constant, ν is the frequency of the incident photon and E_B is the binding energy of the electron. If the energy of the incident photon is higher than the binding energy of the K-shell, this process has the biggest cross section in the K-shell. Therefore, the emptied inner shell will be filled with an outer shell electron.

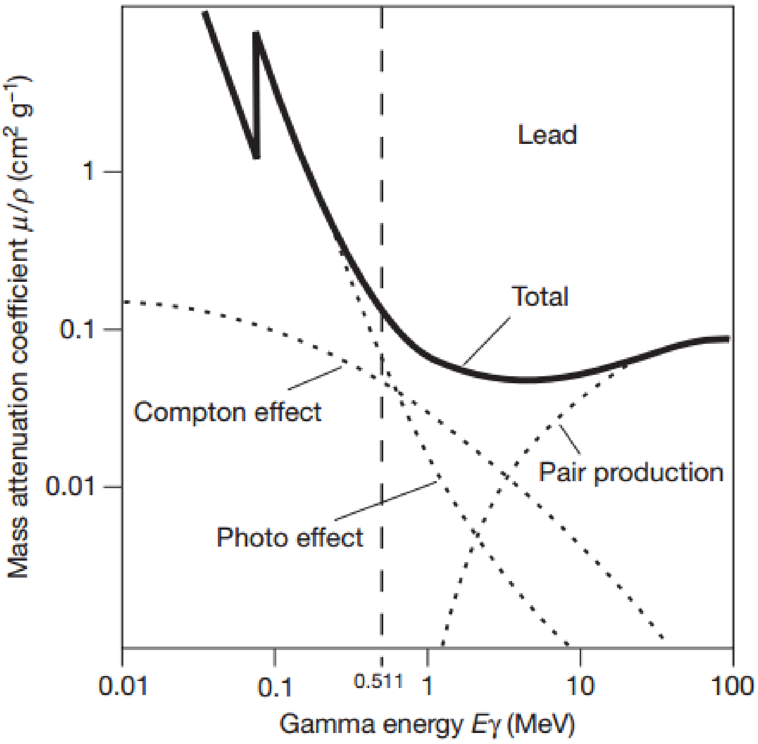

Figure 2.1: Mass attenuation coefficient in lead dependent on incident photon energy. At low energies until ≈ 100 keV the photoelectric effect is the most important effect. For energies of ≈ 1 MeV the Compton effect has the greatest influence. For energies ≫ 1 MeV pair-production effect dominates the mass attenuation coefficient. At 511 keV, the photoelectric effect and Compton effect are of the same magnitude. [2]

Now either X-rays with the energy of this gap can be emitted or the energy can be used to emit another electron of the same atom. This electron is called an Auger electron. The energy of Auger electrons is small in comparison with the primarily emitted electrons. The non-relativistic cross section for the photoelectric effect in the K-shell can be calculated in the non-relativistic Born approximation [4]:

$$\sigma^K_{Photo} = \left(\frac{32}{\epsilon^7}\right)^{\frac{1}{2}} \alpha^4 Z^5 \sigma^e_{Th} \tag{2.14}$$

Where $\epsilon = \frac{E_\gamma}{m_e c^2}$ is the reduced photon energy, $\sigma^e_{Th} = \frac{8}{3}\pi r_e^2$ is the Thompson cross section (elastic scattering), r_e is the classical electron radius, $\alpha \approx \frac{1}{137}$ and Z is the atomic number. The cross section of the photoelectric effect is proportional to the 5th power of the atomic number which leads to a large cross section in dense (high

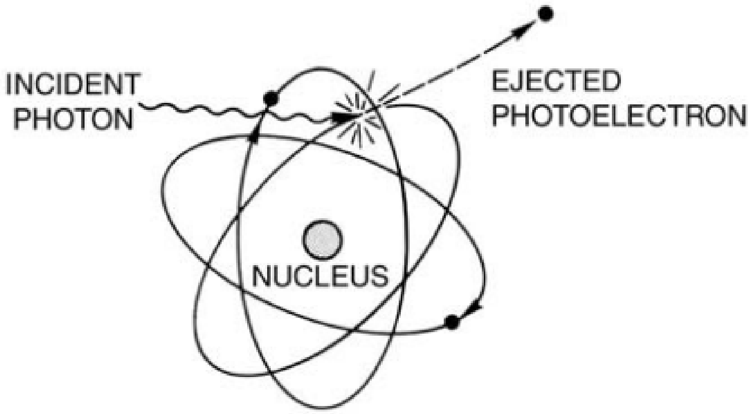

Figure 2.2: Representation of the photoelectric effect. The incident photon gets absorbed by a bound electron and the electron is ejected. [1]

Z) materials like lead.

Compton Effect

The Compton effect describes the inelastic scattering of photons and quasi-free electrons in interaction with matter. A quasi-free electron is a bound electron whose binding energy can be neglected when compared to the energy of the incident photon. While scattering at the electron, the photon changes its direction and loses some of its energy. The lost energy is transferred to the kinetic energy of the electron and is dependent on the angle θ_c between the scattered and the incident photon. An schematic representation of this process can be seen in figure 2.3. The energy of the scattered photon E'_γ can be calculated as [4]:

$$E'_\gamma = \frac{h\nu}{1 + \epsilon_\gamma (1 - \cos\theta_c)} \tag{2.15}$$

Where $\epsilon_\gamma = \frac{E_\gamma}{m_e c^2}$ is the reduced photon energy. In case of a back-scattering ($\theta_c = 180°$) the energy transfer to the electron has its maximum. The cross section σ_c of

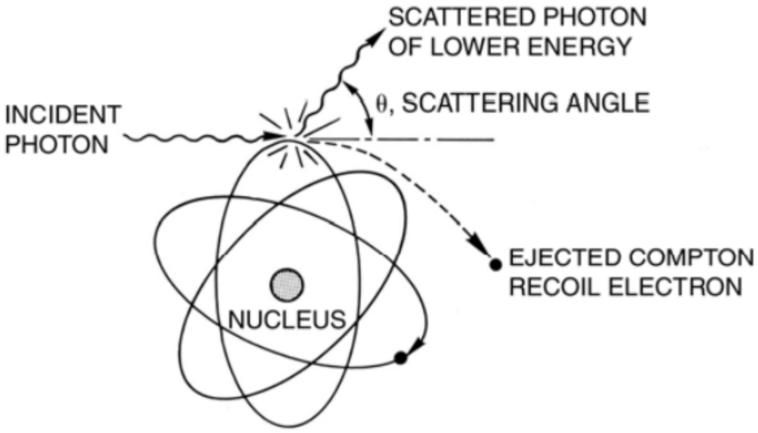

Figure 2.3: Representation of the Compton scattering. The incident photon gets scattered and transfers a part of its energy to the electron. The direction of the photon is changed during the process. [1]

Compton scattering was calculated by Klein and Nishina [4]:

$$\sigma_c = 2\pi r_e^2 [\left(\frac{1+\epsilon_\gamma}{\epsilon_\gamma^2}\right)\left\{\frac{2(1+\epsilon_\gamma)}{1+2\epsilon_\gamma} - \frac{\ln(1+2\epsilon_\gamma)}{\epsilon_\gamma}\right\} + \frac{\ln(1+2\epsilon_\gamma)}{2\epsilon_\gamma} - \frac{1+3\epsilon_\gamma}{(1+2\epsilon_\gamma)^2}] \tag{2.16}$$

As it can be seen, the formula is independent of the atomic number Z. For an atom with Z electrons the cross section σ_c^{atom} is calculated as [4]:

$$\sigma_c^{\text{atom}} = Z\sigma_c \tag{2.17}$$

Only a part of the energy is transferred to the electron. Hence, it is possible to separate the total cross section in a scattering (σ_c^s) and an absorbing part (σ_c^a), which refers to the probability to transfer an energy of $E_{\text{kin}} = E'_\gamma - E_\gamma$ to the electron. The cross sections are given by [4]:

$$\sigma_c^s = \frac{E'_\gamma}{E_\gamma}\sigma_c \tag{2.18}$$

$$\tag{2.19}$$

$$\sigma_c^a = \sigma_c - \sigma_c^s \tag{2.20}$$

Pair Production

In pair production, the photon energy is used to create a pair of particles in the Coulomb field of a nearby atom. In case of the Coulomb field of a nucleus (pair production in Coulomb field of electron is suppressed), the photon needs to provide the energy for two electrons and the recoil to the nucleus. Therefore, the photon needs to exceed a threshold [4]:

$$E_\gamma \geq 2m_ec^2 + 2\frac{m_e^2}{m_{\text{nucleus}}}c^2 \approx 2m_ec^2 \tag{2.21}$$

The threshold to create a pair of an electron and a positron is $2 \cdot m_ec^2 = 2 \cdot 511\,\text{keV} = 1022\,\text{keV}$. Above this threshold the cross section rises until it reaches an energy independent maximum. In PET, the energy of the annihilation photons is 511 keV and pair production does not take part.

2.3 Basics of Positron Emission Tomography

2.3.1 Tracer

Positron Emission Tomography (PET) is a modality to visualize the radioactive β^+-isotope distribution in a volume. A more detailed overview of PET can be found in [1]. This radioactive distribution can either be given through simple sources of radioactive isotopes like a spherical source or through radioactive tracer molecules. Besides the radioactively labeled tracer there are also other kinds of tracers. In general tracers are molecules inside an organism, which are changed in a way that they send information outside of this organism. A radioactive tracer is a compound, which is labeled by a radioactive molecule (tagging). These tracers can follow metabolic processes in an organism allowing to obtain information of these processes. Before it can be used it needs to be part of a liquefied solution, which will then be injected into the organism of interest. This work does not include living organisms. Hence, instead of a tracer, the source used in this work will be a spherical radioactive ^{22}Na source.

2.3.2 Positronium and Annihilation

In this section, it shall be discussed how the positron is used in PET and which consequences follow from these principles. The energy liberated by β^+-decay is mainly transferred to the positron and the electron neutrino. The energy transferred to the positron is therefore dependent on the mother nucleus and the emission angle. While propagating through matter the positron gets rapidly decelerated due to inelastic scattering on nearby bound electrons. After a certain distance (positron range) the kinetic energy of the positron is in range of a local electron and they can form a hydrogen-like state called positronium. Table 2.1 shows positron ranges for different isotopes in water. There are two kinds of positronium, which differ in their spin and half-life: Ortho- and parapositronium. The electron spins of orthopositronium are parallel. It is the triplet state of positronium. The mean lifetime of this state is $14 \cdot 10^{-7}\,\mathrm{s}$. [7] Due to momentum- and spin conservation it decays into an uneven amount of photons with mostly three photons. The electron spins of parapositronium are anti-parallel. Parapositronium is the singlet state of positronium. It has a mean lifetime of $1,25\cdot 10^{-10}\,\mathrm{s}$ [7]. It decays into an even amount of photons, where the leading decay is into two photons. This is the dominant decay and the relevant decay for PET. The probability for an emission process of higher order (more than two photons) is only 0.003% [1]. The two photons can be detected, and therefore a line can be defined on which the annihilation has happened. This line is called a line of response (LOR). By measuring millions of events and filtering out those events, which hit two detectors in a short time window (coincidences), it is possible to calculate an approximately correct image of the spatial distribution of a tracer by use of reconstruction techniques. Hence, orthopositronium is an undesirable state for PET, because PET uses only two photons to create a LOR. Caused by energy conservation, each of these two photons has an energy of 511 keV, which equals the energy of an electron mass. In the case that the positronium is at rest (center of mass system) the momentum conservation leads to an emission under an angle of 180° (back-to-back emission) for the two photons. In reality the positronium has a kinetic energy when annihilating. This leads to a deviation of the emission angle of back-to-back emission due to momentum conservation which can be described through a Gaussian distribution with a full width half maximum (FWHM) of $\approx 0.5°$ [1]. This effect is called non-colinearity. The blurring Δ_{nc} of an image caused by non-colinearity can be approximated [1]:

$$\Delta_{nc} = 0.0022D \tag{2.22}$$

Here, D is the diameter of the PET scanner. As it can be seen, the error increases linearly with increasing diameter. While the positron range is an effect that can not be changed this error can be reduced by the geometry of a PET scanner.

Table 2.1: Properties of different β^+-emitters, the positron range is dependent on the positron energy; [8]

Isotope	Half-Life	Maximal Positron Energy	Mean Range in Water in mm	Max Range in Water in mm
^{11}C	20.7 min	970 keV	1.1	4.1
^{13}N	9.96 min	1.19 MeV	1.5	5.1
^{15}O	124 s	1.72 MeV	2.5	7.3
^{18}F	109.7 min	635 keV	0.6	2.4
^{64}Cu	12.8 h	653 keV	0.7	2.7
^{68}Ga	68 min	1.9 MeV	2.9	8.2
^{76}Br	16.1 h	3.68 MeV	6.4	15.4
^{82}Rb	75 s	3.4 MeV	5.9	14.1

Event Types of a PET System

In PET, photons can be detected by a detector ring surrounding the source. If a photon is detected, an event is triggered. There are five possible event types. Figure 2.4 shows different event types which can occur. In the case that in a given time window (coincidence window) after a triggered event no second photon is detected, the event type is assigned as a single event. Single events are not further analyzed. Approximately 90% or more of all triggered events are single events [1]. In case that a second event is detected in the time window, the event type is called coincidence. A true coincidence is the preferred event type. In this case the two photons that are emitted by the annihilation are directly detected. They neither have their direction changed, nor lose energy before the detection happens. In a scattered coincidence, one or both detected photons become scattered along their path. During the scattering process, the direction of the photon is changed and the energy reduced. The two detected photons are determining a false LOR which leads to low contrast. In random coincidences, two photons, of different origins, are measured in the same coincidence window and therefore are interpreted as real events. Because they are unrelated, they do not carry any spatial information with regard to the activity distribution of the object of interest. The background detection rate N_R due to random coincidences can be calculated as [1]:

$$N_R = 2\tau N_1 N_2 \tag{2.23}$$

Where N_1 and N_2 are the detection rates of a pair of detectors. τ is the coincidence window. The factor 2 in the equation is referring to the fact that both detectors can trigger a gate to build a coincidence. In case that only one detector is used as trigger the rate of random is given by:

$$N_R = \tau N_1 N_2 \tag{2.24}$$

In addition to the mentioned coincidence cases, it is possible that a multiple coincidence happens, which means that two photons are measured during the coincidence window. In most PET systems these events are not considered as true events.

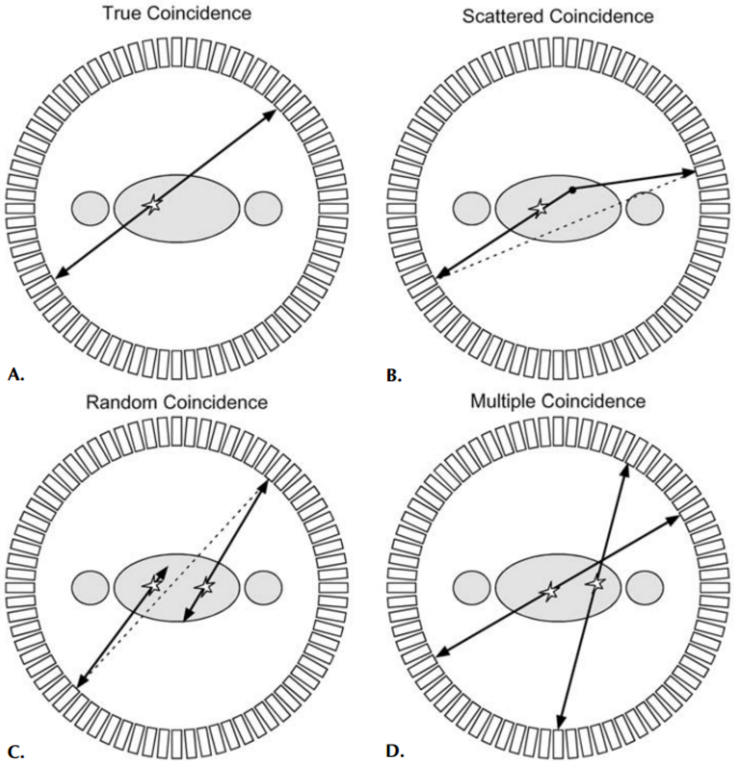

Figure 2.4: Figure of different coincidence types. True events are the events of choice. However, scattered events and random events will be measured and lead to a blurring effect. [1]

2.4 Gas Detectors

The detector modules used in the HIDAC are special gas detectors called Multi-Wire-Proportional-Chambers (MWPC). A gas detector is a chamber, in which incident radiation ionizes gas molecules inside of the detector, and thereby, creates pairs of ions and electrons. These charges get separated and the resulting charge signals, on the cathode or anode, are measured. To understand the detection principle of a MWPC, a cylindrical detection chamber with an anode wire along its axis will be discussed. The electric field in a cylindrical chamber as function of the distance from the cylindrical axis r is given by: [5]

$$E(r) = \frac{U_0}{r \ln(r_a/r_i)} \tag{2.25}$$

U_0 is the applied voltage, r_a is the radius of the gas chamber and r_i is the radius of the anode wire. Incident radiation ionizes a gas atom inside the chamber and

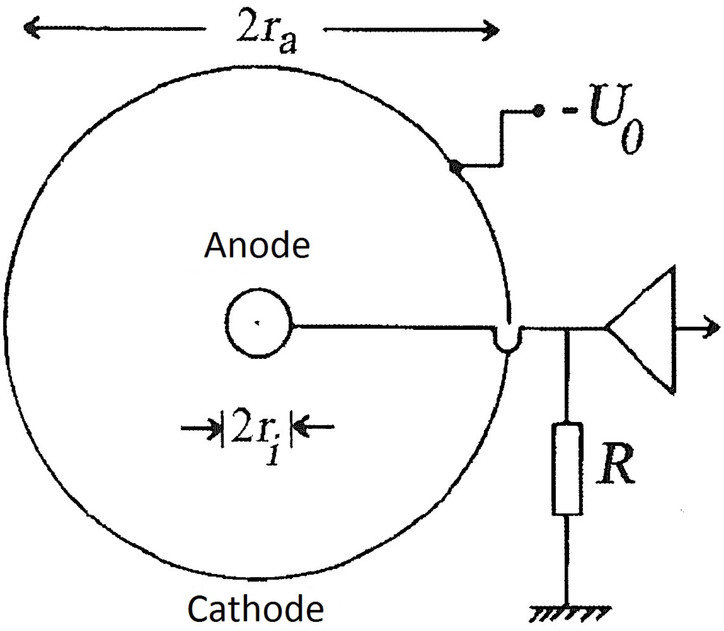

Figure 2.5: Cylindrical ionization chamber [5]

creates an electron-ion-pair. For low electric fields the ion drifts to the cathode, while the electron drifts to the anode wire. The voltage pulse ΔU^- created by the collected electrons is given by: [5]

$$\Delta U^- = -\frac{Ne}{C}\frac{\ln(r_0/r_i)}{\ln(r_a/r_i)} \tag{2.26}$$

And the voltage pulse ΔU^+ created by the drifting ions is given by: [5]

$$\Delta U^+ = -\frac{Ne}{C}\frac{\ln(r_a/r_0)}{\ln(r_a/r_i)} \tag{2.27}$$

In the case that ions are moving with a velocity $v = \mu E$ towards the tube wall, the ion trajectory can be described by: [9]

$$\frac{dr(t)}{dt} = \mu\frac{U}{r\ln(r_a/r_i)} \tag{2.28}$$

Where μ is the mobility of the ions in the gas. The equation leads to: [9]

$$r(t) = r_i \sqrt{1 + \frac{t}{t_0}} \tag{2.29}$$

and:

$$t_0 = \frac{r_i^2 \ln(r_a/r_i)}{2\mu U} \tag{2.30}$$

2.4.1 Proportional Counting Tube

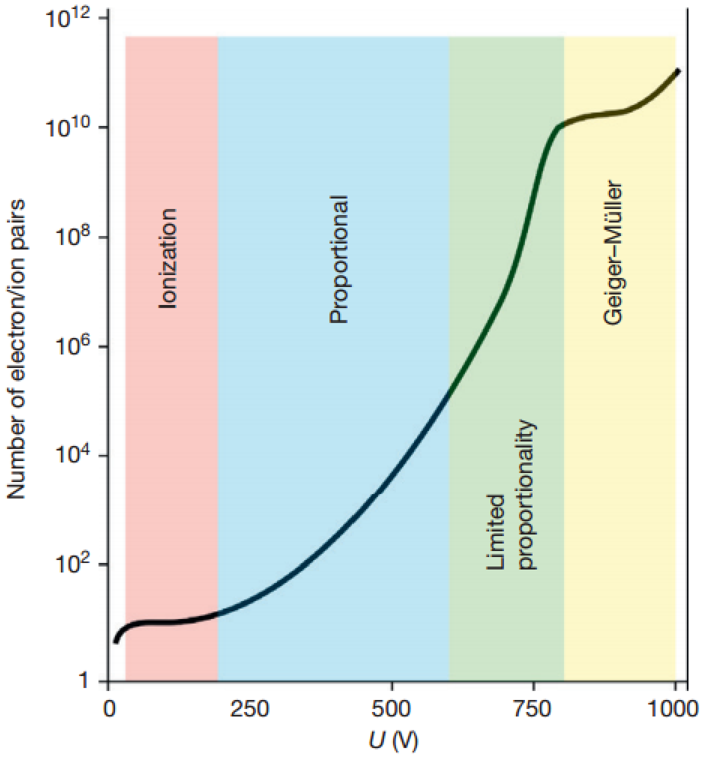

Figure 2.6: The image shows different operating regions of a counting tube. The regions are dependent on the used voltage. In the proportional region the signal magnitude is proportional to the incident radiation. If the voltage is further increased a region of non-proportionality is reached. [2]

Gas chambers can operate in different voltage regions. A schematic image of these regions dependent on the applied voltage can be seen in figure 2.6. The behavior in small voltage regions is described above. If the voltage is increased or the wire radius is reduced (electric field $\propto \frac{1}{r}$), the proportional region is reached. In this region, the measured signal magnitude is proportional to the incident radiation energy. If the Geiger-Mueller region is reached, a high gain is obtained, but the proportionality is lost. In a Proportional Counting Tube (proportional region) the voltage used is large enough that electrons created during the primary ionization process gather enough kinetic energy between two impacts with gas atoms to ionize these secondary gas atoms. In this case, the kinetic energy ΔT_{kin} gained by the electric field between two impacts at radii r_1 and r_2 needs to be greater than the ionization energy of the gas. ΔT_{kin} is given by [5]

$$\Delta T_{\text{kin}} = e \int_{r_1}^{r_2} E(r)dr = eU_0 \frac{\ln(r_2/r_1)}{\ln(r_a/r_i)} \tag{2.31}$$

$$\tag{2.32}$$

The ionization due to particles, which have been initially created (primary electrons), is called secondary ionization. A chain of secondary ionization processes is called avalanche and the signal pulse ΔU produced by this effect at the anode wire can be calculated by

$$\Delta U = -A\frac{Ne}{C} \tag{2.33}$$

Where N is the number of produced electrons and C is the capacity of the counting tube. A is called the gas amplification factor. In the proportional voltage area, A is constant. Therefore, the signal is directly proportional to the energy of the incident particle. In gas mixtures the number of primary created electrons can be further increased due to the Penning effect [10]. This effect can occur, if the metastable excitation energy of a gas component is higher than the ionization energy of the other gas component. Electron collisions lead to atoms in this excited metastable state which ionize the atoms of the other gas by collision.

$$A^* + B \rightarrow A + B^+ + e^- \tag{2.34}$$

The number of electron-ion-pairs created per distance (in cm) is called first Townsend-Coefficient α. If N is the atom density of noble gases and σ_i is the cross section, α

can be calculated as [5]

$$\alpha = \sigma_i N = \frac{1}{\lambda} \tag{2.35}$$

Where λ is the free path length of electrons in the gas. When N_0 is the number of primary created electrons, the number of electrons $N(x)$ after a given distance x can be described through [4]

$$N(x) = N_0 \exp(\alpha x) \tag{2.36}$$

The Townsend Coefficient is dependent on the electric field and therefore on the position in the counting tube. [4]

$$N(x) = N_0 \exp(\int \alpha dx) \tag{2.37}$$

Using the first Townsend Coefficient, the amplification factor can be calculated. [4]

$$A = \exp(\int_{r_k}^{r_i} \alpha(x) dx) \tag{2.38}$$

The value r_k is the distance from the center, in which the secondary ionization is starting. If recombination of ions, electron attachment at atoms and ionization through photons created by the decay of exited atoms is neglected, the gas amplification in dependence of the applied voltage U_0 can be approximated by: [5]

$$A \propto \exp\left[k\sqrt{U_0}\left(\sqrt{\frac{U_0}{U_S}} - 1\right)\right] \tag{2.39}$$

k is a constant and U_S is the threshold voltage to reach the proportional region. If the current signal $i(t)$ of a single incident photon at the wire is integrated, the amplified charge Q can be measured and therefore the amplification factor can be calculated [4]

$$Q = \int i(t) = eN_0 A \tag{2.40}$$

During the avalanche, photons will be created. These photons can themselves ionize gas molecules and have an additional effect on the amplification. If an electron has the probability γ to create additional electron, the new amplification factor A_γ can be derived by [4]

$$A_\gamma = \frac{A}{1 - \gamma A} \tag{2.41}$$

γ is called second Townsend Coefficient. As soon as the applied electric field is being effected by the created electrons, saturation effects occur. For $A_\gamma \to 1$ the signal pulse becomes independent of the primary ionization. The high electric field needed is realized by thin central wires. The avalanche takes place close to the wire, where the electric field becomes high enough. The ratio R of the signals heights of the moving ions U^+ and electrons U^- can be calculated with [4]

$$R = \frac{U^+}{U^-} = \frac{\ln(r_a/r_0)}{\ln(r_0/r_i)} \tag{2.42}$$

An illustration of the avalanche process can be seen in 2.7. At first an electron-ion-pair is created. The ion drifts to the cathode while the electron drifts towards the anode wire. When the electric field in neighborhood of the anode wire becomes so large that secondary ionization occurs an avalanche is created. While the ions are drifting towards the cathode and the electrons are accelerated towards the anode wire they build a drop like distribution around the wire. The electrons are absorbed by the wire while the ions are still in neighborhood of the wire and drift towards the cathode.

2.4.2 Multi-Wire-Proportional-Chamber

The Multi-Wire-Proportional-Chamber (MWPC) is based on the principles of a proportional tube but extends these. A simple MWPC is like a proportional tube but uses multiple wires which are arranged parallel to each other. In contrast to a tube, the outer shape of a simple MWPC is a cuboid. Two opposed planes are used as cathodes and the anode wires are arranged parallel to these planes as shown in figure 2.8. Every wire in the MWPC can be seen as an independent detector. The signal magnitudes measured at the anode wires can be used to get spatial information of the incident radiation. A common method to measure the position of a signal is the use of segmented cathodes, where the induced signal can be measured. For example the cathode can be separated into parallel strips (pads) which can be seen in figure 2.9. The measured induced signals can be used to determine the

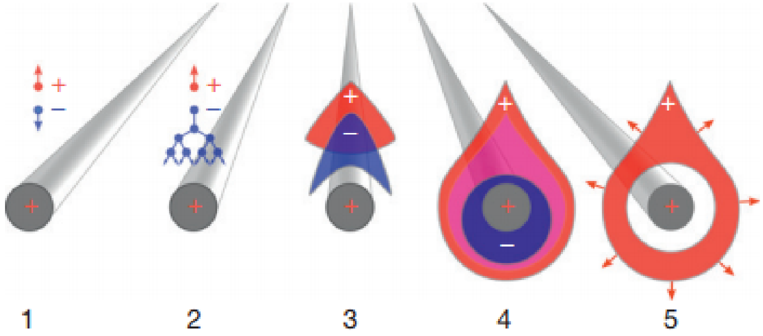

Figure 2.7: Avalanche process: (1) Primary ionization creates an ion-electron-pair. Electrons are drifting towards the wire and ions are drifting towards cathode; (2) The electric field becomes so large, that an avalanche occurs. (3) and (4) the created ions and electrons are building a drop like shape around the wire. (5) The electrons become absorbed by the wire and the ion cloud remains and drifts to the cathode. [2]

charge center. Hence, a charge displacement can be calculated for every measured event. If the distance between two wires (pitch) is d, the spatial standard deviation orthogonal to the wires $\sigma(x)$ (pads parallel to wires) is given by [4]

$$\sigma(x) = \frac{d}{\sqrt{12}} \tag{2.43}$$

Signal Creation

The induced signals are created by moving charges inside of the detector. A thourough discussion of this phenomenon can be found in [9]. At first the signal on the wires shall be discussed. A point charge q at position $z = z_0$ induces a charge on electrically conducting surfaces like metals. The electric field $\vec{E} = (E_x, E_y, E_z)$ on the metal surface is given by [9]

$$E_z(x, y) = -\frac{q z_0}{2\pi\epsilon_0(x^2 + y^2 + z_0^2)^{\frac{3}{2}}} \tag{2.44}$$

The electric field components E_x and E_y are zero. The total charge Q induced in an electrically conducting plate can be calculated with help of the surface charge density

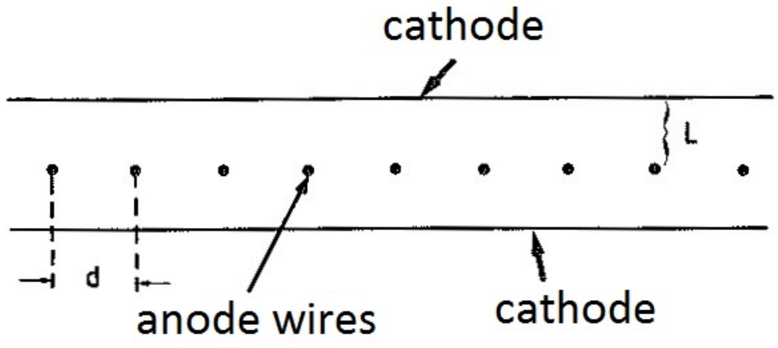

Figure 2.8: Image of a simple MWPC. The anode wires are parallel to the cathode planes and parallel to each other with distance d. [4]

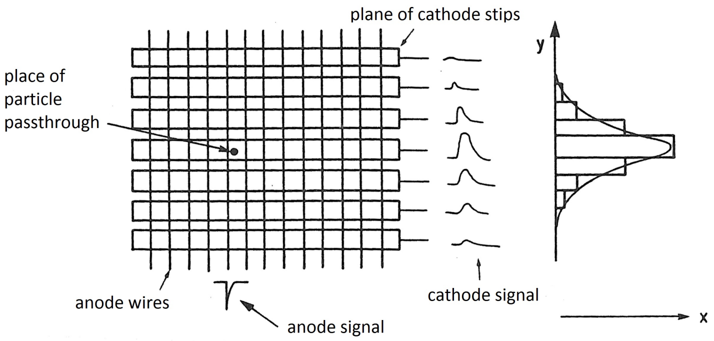

Figure 2.9: The cathodes are separated in cathode tracks which can measure the induced signal. [4]

$\sigma(x,y) = \epsilon_0 E_z(x,y)$: [9]

$$Q = \int_{-\infty}^{\infty}\int_{-\infty}^{\infty} \sigma(x,y)dxdy = -q \tag{2.45}$$

If the surface is divided into several grounded strips of width w, each strip i carries a portion of the total charge Q_i. In this case the surface charge density is integrated over the area of the strip (infinitely long strips). In the case of the central strip, the partial charge Q_1 can be calculated as [9]

$$Q_1(z_0) = \int_{-\infty}^{\infty}\int_{-\frac{w}{2}}^{\frac{w}{2}} \sigma(x,y)dxdy = -\frac{2q}{\pi}\arctan(\frac{w}{2z_0}) \tag{2.46}$$

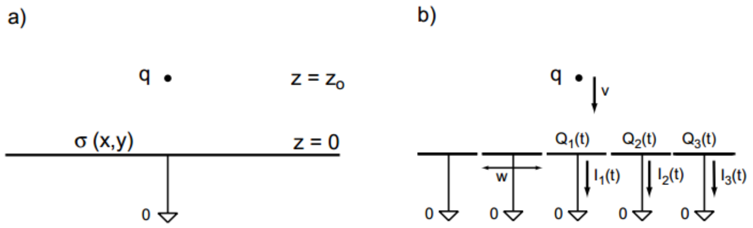

Figure 2.10: Image of surface density. In (a) the metal plane is infinitely large. The induced charge equals the inducing charge. In (b) the surface is separated in strips. The induced charge is dependent on the position and width of the strips. An induced current is measured when the charge is moving. [9]

In contrast to the induced charge of an infinite metal surface, the induced charge is dependent on the distance of the point charge to the cathode strip z_0. If the charge is moving towards the cathode strip with a given velocity v ($z_0(t) = z_0 - vt$) the corresponding induced current I_1^{ind} can be derived with [9]

$$I_1^{ind} = -\frac{d}{dt}Q_1[z_0(t)] = \frac{4qw}{\pi[4z_0(t)^2 + w^2]}v \tag{2.47}$$

If each wire in a MWPC is infinitely long and has the potential U_n, the carried charge q_n of a given wire n is given by a capacitance matrix c_{nm} (both per length unit) [9]

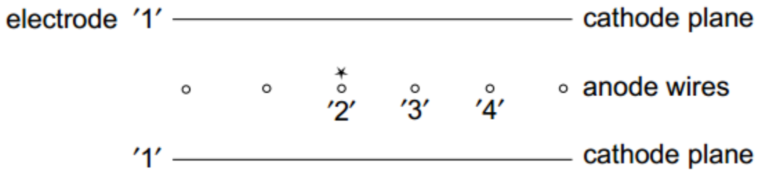

Figure 2.11: Image of the labeling of a MWPC. [9]

$$q_n = \sum_{m=1}^{N} c_{nm}U_m \tag{2.48}$$

Both cathode planes are labeled electrode 1 and the wires are labeled as electrodes 2, 3, etc. which can be seen in figure 2.11. This results in an electric field of [9]

$$E(r) = \frac{q_n}{2\pi\epsilon_0 r} = \frac{1}{2\pi\epsilon_0 r}\sum_{m=1}^{N} c_{nm}U_m \tag{2.49}$$

Where r is the distance from n-th wire and is small compared to the distance between chamber electrodes. In this case the trajectory is the same as in the drift tube, described by equations 2.28, 2.29 and 2.30 [9]

$$r(t) = r_i\sqrt{1 + \frac{t}{t_0}} \tag{2.50}$$

and

$$\frac{1}{t_0} = \frac{\mu}{r_i^2\pi\epsilon_0}(\sum_{m=1}^{N} c_{nm}U_m) \tag{2.51}$$

With the trajectory given, the weighting fields of the wires need to be considered to find the induced current signals. To achieve this, a wire i of choice is set to voltage V_w while all other wires are on ground potential. The sum of all wires leads to the current I_w

$$I_w = -\frac{N_{tot}e_0}{4\pi\epsilon_0}\frac{C_{12}}{t + t_0} \tag{2.52}$$

N_{tot} is the number of ions with charge e_0 and C_{12} is the capacity between electrode 1 and 2 (cathode plane and anode wire). If all wires have the same voltage, t_0 becomes

$$\frac{1}{t_0} = \frac{\mu U C_{12}}{a^2\pi\epsilon_0} \tag{2.53}$$

As the previous discussion was about signals measured at the anode wires, the following discussion is about the induced signals on the cathode strips. An image of a gas chamber with several cathode strips can be seen in figure 2.12. The wire pitch is given by s, the distance from the cathode-plane to the wires is given by $h = D$ and the width of a strip w is given by $w = 2a$. In enclosed systems, the sum of all signals is zero. Hence, the induced signals on the cathode pads I_c equals the negative signals measured on the wires I_w. For one cathode plane I_{c1}, the signal is

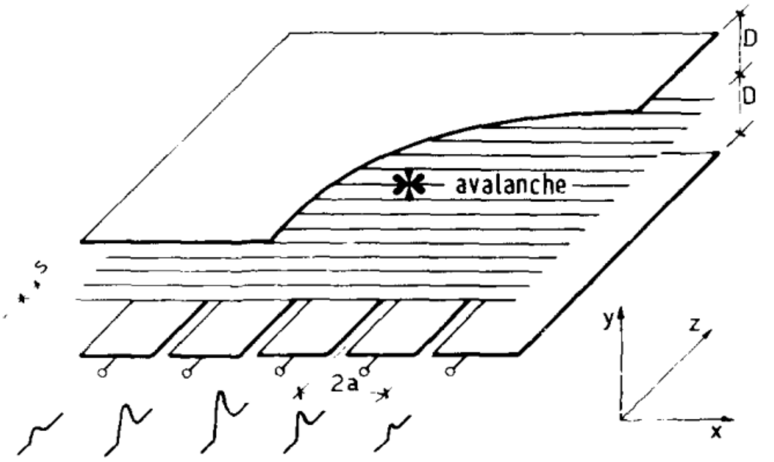

Figure 2.12: Image of a gas detector. The cathodes are divided into several strips. The distance from the cathodes to the wires is D, the wire pitch is s and the strip width is $2a$. [11]

given by [9]

$$I_{c1} = \frac{1}{2} I_c = -\frac{1}{2} I_w = \frac{1}{2} \frac{N_{tot} e_0}{4\pi\epsilon_0} \frac{C_{12}}{t + t_0} \tag{2.54}$$

Analogous to the weighting fields of the wires, a weighting field for the cathode pads can be measured. A simplified method to calculate the signal on a strip was invented in [11] [12]. At first, the signal gets calculated for a strip of infinitesimal width. The signal then gets integrated over the given strip width. During the calculation the cathode charge distribution $\Gamma(\lambda)$ is defined, where $\lambda = \frac{x}{D}$ is the distance of the infinitesimal strip from the avalanche position. x is the position on the cathode plane parallel to the wires. $\Gamma(\lambda)$ is defined through

$$dI_{c1}(t, h) = I_c(t)\Gamma(\lambda)d\lambda \tag{2.55}$$

$$\int_{-\infty}^{\infty} \Gamma(\lambda)d\lambda = \frac{1}{2} \tag{2.56}$$

Gatti et al introduced a semi-empirical expression to calculate $\Gamma(\lambda)$

$$\Gamma(\lambda) = K_1 \frac{1 - \tanh^2(K_2\lambda)}{1 + K_3 \tanh^2(K_2\lambda)} \tag{2.57}$$

The parameters K_1 and K_2 are defined with help of K_3.

$$K_1 = \frac{K_2\sqrt{K_3}}{4\arctan(\sqrt{K_3})} \tag{2.58}$$

$$K_2 = \frac{\pi}{2}\left(1 - \frac{\sqrt{K_3}}{2}\right) \tag{2.59}$$

K_3 is dependent on the geometry of the detector chamber. Figure 2.13 shows the K_3 for different geometries. The signal $I(t,\lambda,w)$ on a given strip of width w, which is centered at position λ, can be calculated by integrating 2.55 [9]

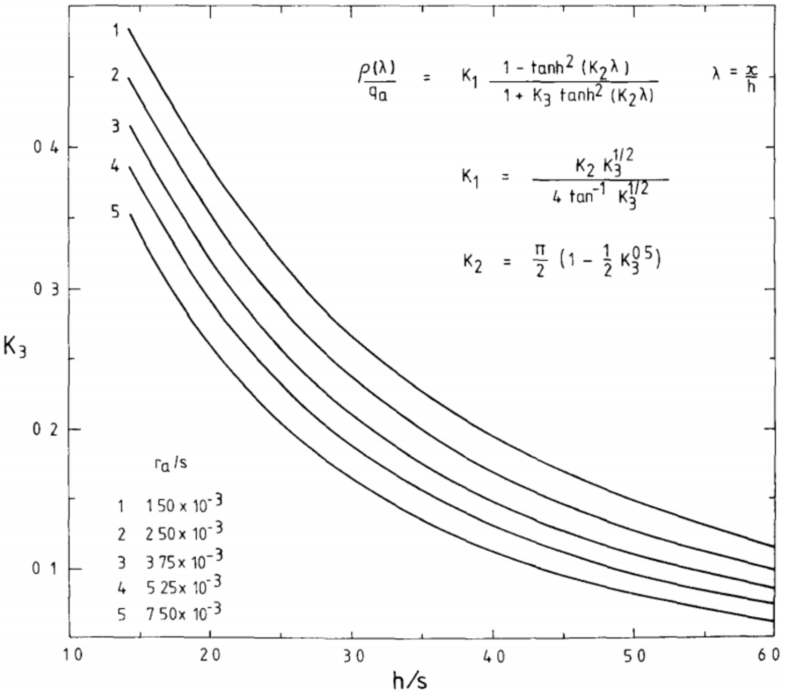

Figure 2.13: Parameter K_3 dependent on different chamber geometries. h is the distance from the cathode to the anode and s is the pitch from wire to wire. r_a is the radius of a given wire. [12]

$$I(t,\lambda,w) = I_c\int_{\lambda-w/2}^{\lambda+w/2}\Gamma(\lambda')d\lambda' = I_c(t)P_0(\lambda) \tag{2.60}$$

with

$$P_0(\lambda) = \frac{K_1}{K_2\sqrt{K_3}}(\arctan\left[\sqrt{K_3}\tanh(K_2(\lambda + \frac{w}{2}))\right] - \arctan\left[\sqrt{K_3}\tanh(K_2(\lambda - \frac{w}{2}))\right]) \tag{2.61}$$

$P_0(\lambda)$ is called Pad Response Function (PRF).

Displacement

As described in the previous section, the PRF $P_0(\lambda) = I_i(t)/I_{tot}(t)$ defines the fraction of the total signal measured on a cathode strip. By measuring the signal magnitudes on nearby pads, the position of the signal origin and therefore the displacement of the position of the pad with maximal signal height can be calculated. The measured signal is the superposition of multiple avalanches. Therefore, the effective P_{eff} results from folding the distribution of the avalanche positions λ_i, which contribute to the cathode signal. As a first approach, it is sufficient to use a superposition of Gaussian signals. [9] The measured signals of the i-th pad are $I_i(t)$. For three nearby pads the quotients are given by [9]

$$\frac{I_2(t)}{I_1(t)} = p_1 = \frac{P_0(\lambda_1)}{P_0(\lambda_1 - w)} \tag{2.62}$$

$$\frac{I_2(t)}{I_3(t)} = p_2 = \frac{P_0(\lambda_2)}{P_0(\lambda_2 + w)} \tag{2.63}$$

The avalanche position can be calculated by finding λ_1 and λ_2. With the common chosen relative weighting factors p_1^2 and p_2^2 [9] the weighted position of the avalanche λ can be calculated [9]

$$\lambda = \frac{1}{p_1^2 + p_2^2}\left(p_1^2\lambda_1 + p_2^2\lambda_2\right) \tag{2.64}$$

Several different approaches to calculate the displacement have been discussed in [13]. In the case of a Gaussian approximation, the signal on the i-th pad inside a coordinate system shown in figure 2.12 can be approximated by

$$I_i(\lambda) \approx A\exp\left(-\frac{x}{2\sigma}\right) \tag{2.65}$$

In this approximation, A is the magnitude of the Gaussian function, σ its variance and x the centered position of the pad. The measured signals on the $(i-1)$-th, i-th and $(i+1)$-th pad are, therefore, proportional to:

$$I_{i-1} = I_1 \propto \exp\left(-\frac{(x+w)^2}{2\sigma^2}\right) \tag{2.66}$$

$$I_i = I_2 \propto \exp\left(-\frac{x^2}{2\sigma^2}\right) \tag{2.67}$$

$$I_{i+1} = I_3 \propto \exp\left(-\frac{(x-w)^2}{2\sigma^2}\right) \tag{2.68}$$

As I_{i-1}, I_i and I_{i+1} in equation 2.66, 2.67 and 2.68 are measured values and therefore known, the equations can be solved to achieve x and σ. To calculate the unweighted displacement used by [13], the ratios I_{i+1}/I_{i-1} and $I_{I^2}/(I_{i-1}I_{i+1})$ need to be calculated:

$$\frac{I_{i+1}}{I_{i-1}} = \exp\left(\frac{2xw}{\sigma^2}\right) \tag{2.69}$$

$$\frac{I_i^2}{I_{i-1}I_{i+1}} = \exp\left(\frac{w^2}{\sigma^2}\right) \tag{2.70}$$

This leads to the unweighted Gaussian displacement

$$x_{unweighted} = \frac{w}{2}\frac{\ln\left(I_{i-1}/I_{i+1}\right)}{\ln\left(I_{i-1}I_{i+1}/I_i^2\right)}. \tag{2.71}$$

Solving 2.66, 2.67 and 2.68 for σ and x leads to the weighted displacement function of 2.64. To achieve this, the following ratios are calculated

$$\frac{I_i}{I_{i-1}} = \exp\left(\frac{2xw+w^2}{\sigma^2}\right) \tag{2.72}$$

$$\frac{I_{i+1}}{I_i} = \exp\left(\frac{2xw-w^2}{\sigma^2}\right) \tag{2.73}$$

Solving 2.70 for σ gives

$$\sigma^2 = -w^2 \ln\left(\frac{I_{i-1}I_{i+1}}{I_i^2}\right) \tag{2.74}$$

Solving 2.72 and 2.73 for x leads to

$$x_1 = -\frac{w}{2} + \frac{\sigma^2}{w}\ln\frac{I_i}{I_{i-1}} \tag{2.75}$$

$$x_2 = -\frac{w}{2} + \frac{\sigma^2}{w}\ln\frac{I_{i+1}}{I_i} \tag{2.76}$$

Adding these terms with respect to the weighting factors 2.64 gives the desired weighted displacement function

$$\begin{aligned} x_{weighted} = \frac{1}{I_{i-1}^2 + I_{i+1}^2}(I_{i-1}^2 &\left[-\frac{w}{2} + \frac{\sigma^2}{w}\ln\frac{I_i}{I_{i-1}}\right] \\ &+ I_{i+1}^2\left[-\frac{w}{2} + \frac{\sigma^2}{w}\ln\frac{I_{i+1}}{I_i}\right]) \end{aligned} \tag{2.77}$$

The two described displacement functions are the most common ones and will be used in this work. Even though other displacement functions use more pads than three, it has been shown signals measured at pads farther away are negligible.

3 HIDAC

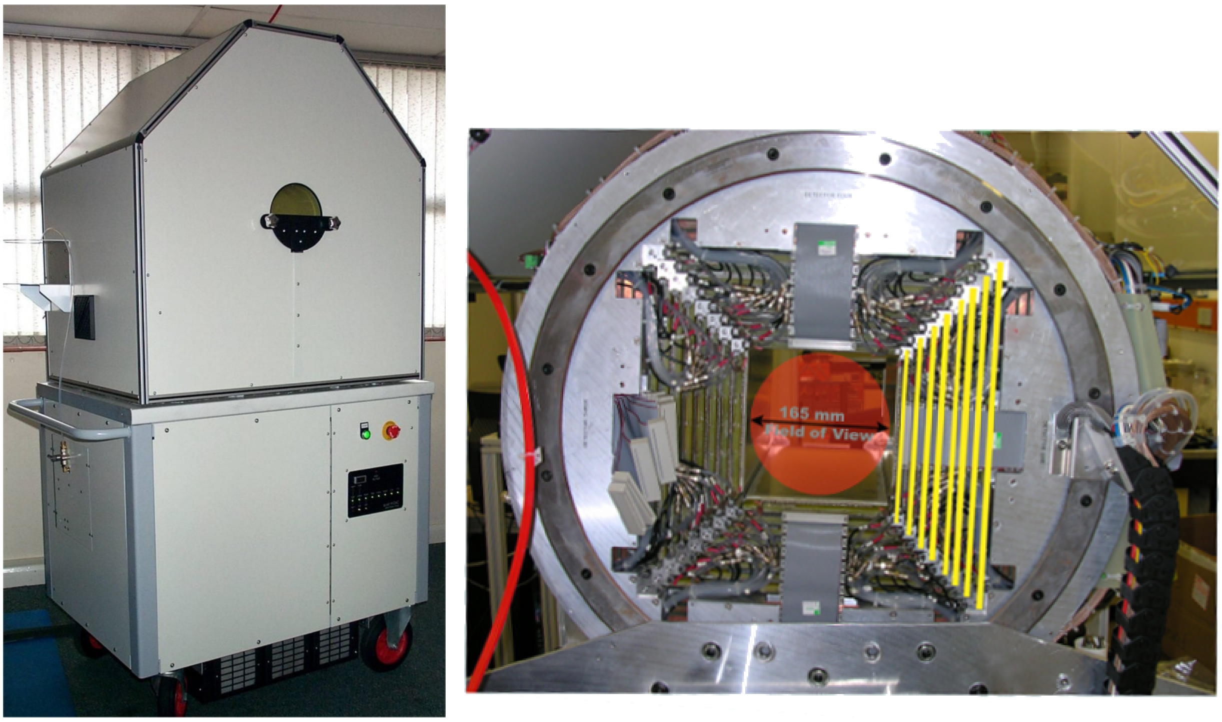

(a) Photograph of HIDAC with cover [14]

(b) Photograph of upper part of HIDAC back without cover [15]

Figure 3.1: Image (a) is a photograph of the commercial HIDAC system. While the upper part holds the detectors and electronic readout, the lower part includes the gas and power supply. (b) upper part HIDAC with removed covers; The red labeled area is the field of view (FOV) and is surrounded by four detector heads which can be separated into several detector modules. The detector gantry can be turned by 180°.

The Small-Animal-PET-Camera in this work is called HIDAC which means High Density Avalanche Chamber. The HIDAC was invented in 1973 by Dr. Alan Jeavons and was sold as a commercial PET system used for small animals by Oxford Positron Systems. Figure 3.1 shows two pictures of the HIDAC system. The HIDAC consists of four detector heads. Each detector head has several detector modules, each functioning as an independent detector. Figure 3.1 (b) shows a photograph of the upper HIDAC (gantry) with the cover removed. The several planar detector modules of one detector head are marked by yellow stripes. The detector ring in this setup is therefore realized by a box made of modules. Enclosed by the four detector heads is a red marked area. This area refers to the sensitive volume of the camera, called the field of view (FOV). Hence, the FOV defines the volume in which the radioactive activity distribution can be measured and analyzed. The FOV of the HIDAC is a cylinder with a diameter of 165 mm and a length of 280 mm. Due to the geometry of the detector it has gaps between the detector heads, which cannot be used to measure photons. To overcome this issue, the whole detector ring can be rotated 180° along its central axis in a time of 6 s for a half rotation in 3180 steps. As can be seen in 3.1(b) the detector modules have different sizes depending on their position inside a detector head. This results in slight differences in the analysis, but the operation is the same for all modules. Figure 3.2 shows a schematic construction of a HIDAC module. Each module is a fully functional MWPC. The MWPCs have $20\,\mu$m thick gold-plated tungsten-rhenium wires with a wire-to-wire distance of 1.5 mm. At the edges, a wire with a thickness of $300\,\mu$m is used. This results in a more homogeneous field. Each module is enclosed by two photon-to-electron converters used to convert incident photons to electrons. Each converter consists out of several layers. The first layer is a plastic layer of 0.2 mm followed by a layer of lead with a thickness of 0.05 mm. These two layers are used to seal the gas inside the module. The two layers are followed by an alternation of sixteen 0.14 mm thick isolation layers and 0.06 mm thick layers of lead. The final layer is a carrier layer with implemented conductor tracks used as cathode strips with a width of 0.7 mm and a strip center to strip center separation of 1.0 mm. The cathode strips of the two converters are perpendicular to each other. Therefore, a readout in two spatial dimensions is possible. The readout direction is always perpendicular to the direction of the tracks. The direction where the tracks are parallel to the wires shall be called the y-direction and the direction where the tracks are perpendicular to the wires shall be called the x-direction. The alternating layers and the carrier layer are perforated with holes of a diameter of 0.4 mm and a distance of 0.5 mm from hole to hole. A common voltage for the wires is around $(+1900 \pm 200)$ V and the voltage for the outer converter layer is around (-2900 ± 300) V while the cathode strips are at zero potential. The lead converter layers are connected with help of a voltage divider which sets the layers to different

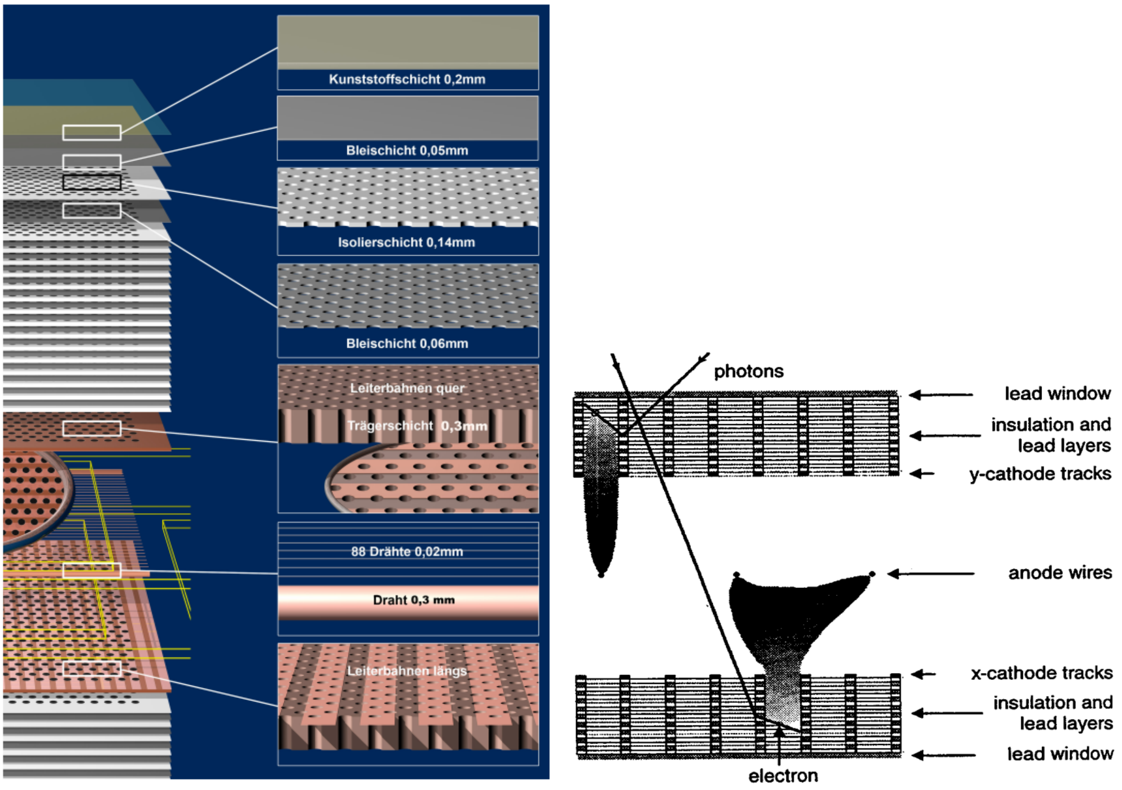

(a) (b)

Figure 3.2: (a) The module has two converters, made out of several layers. The signal can be read out by two perpendicular cathode tracks [15] (b) Schematic image of the HIDAC module. The incident photons create electrons inside of the converters which then drift towards the gas chamber while its yield is increased. After reaching the gas chamber the electrons drift towards the anode wires to create avalanches which can be measured and used as trigger. [10]

voltages. Hence, an electric field is applied inside of the holes. The counting gas used in the HIDAC is a mixture of Argon and Diisopropyl ether (DIPE). Figure 3.2(b) gives an image of the HIDAC principle. Due to the Compton and photoelectric effect, as discussed in section 2.2.2, the incident rays from the volume of interest may interact with the lead in the converters and may be converted into an electron. This electron has a chance to reach a hole inside of the perforated converter. The electric field inside of the holes filled with the gas mixture performs three purposes: While it helps the electrons to drift to the gas chamber, it amplifies its yield and focuses the electrons to the center of the hole [10]. After reaching the inner chamber volume, the electrons are drifting towards the anode wires and create avalanches, which have been discussed in section 2.4.1. The HIDAC uses the resulting voltage drop at the anode wire as a trigger to recognize an event. The ion-cloud of an avalanche can be seen in figure 2.7. Caused by the drop-like shape of the ion-cloud, the measured signal on the both cathode planes differs. Comparing the two signal heights gives the information in which converter a γ-ray has been converted. The cathode strips are grouped to reduce the number of channels needed to read out a module. The pads can be separated in groups and blocks. Figure 3.3 shows an illustration of the readout pattern used in the HIDAC. The figure shows two groups (red and green) and three blocks (blue, yellow and purple). Twenty-four nearby cathode strips (pads) form one group. In a group, every second pad is connected to another. The pads not connected to each other (every second) are used for the block information. The i^{th} block connects the ($2i^{\text{th}}$) strip of each group. When a signal is measured an approximate location of the avalanche can be given by analyzing the signal height of the groups. By analyzing the signal heights of the blocks, the position of the avalanche can be calculated as discussed in 2.4.2. While the number of blocks is twelve for every module, the number of groups differ, depending on the number of total pads of a module and therefore on the size of the module.

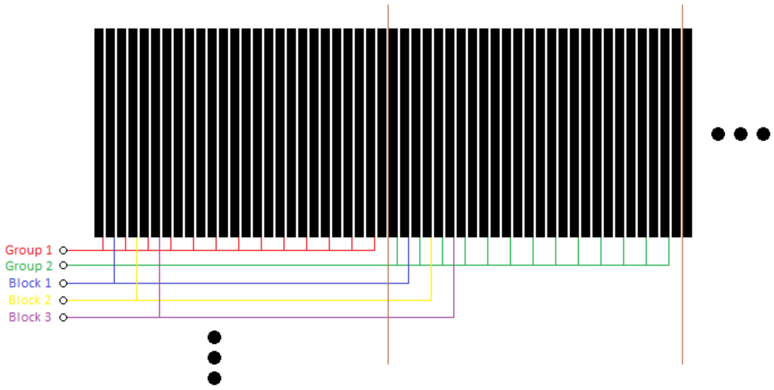

Figure 3.3: Readout pattern of the HIDAC; Groups (red and green) are used to determine the approximate location of the avalanche. The blocks (blue, yellow and purple) are then used to calculate the location of the avalanche.

3.0.1 High Resolution HIDAC

The resolution of the HIDAC has different physical limitations. Due to non-colinearity one of them is the distance between the detector heads shown by equation 2.22.

Therefore, to get a better resolution, it would be beneficial to decrease the distance of the detector heads to each other. To achieve that, a construction (inlet) has been created to reduce the distance for two detector heads, while two detector heads have been removed. An image of the new high resolution HIDAC can be seen in figure 3.4. The construction has multiple benefits. The inlet is fixed inside of the gantry without the need of greater changes to the gantry. It is easily possible to change the HIDAC back to its original state. In addition, it is possible to change the distance of the detectors continuously. This enables an analysis for different detector distances. Either way, the positioning of the detector heads may not be exactly centered inside the gantry. This results in a difference of the rotation axis and a blur in the reconstructed images. To correct this, the reconstruction algorithm has to change the position of the measured events according to the module position.

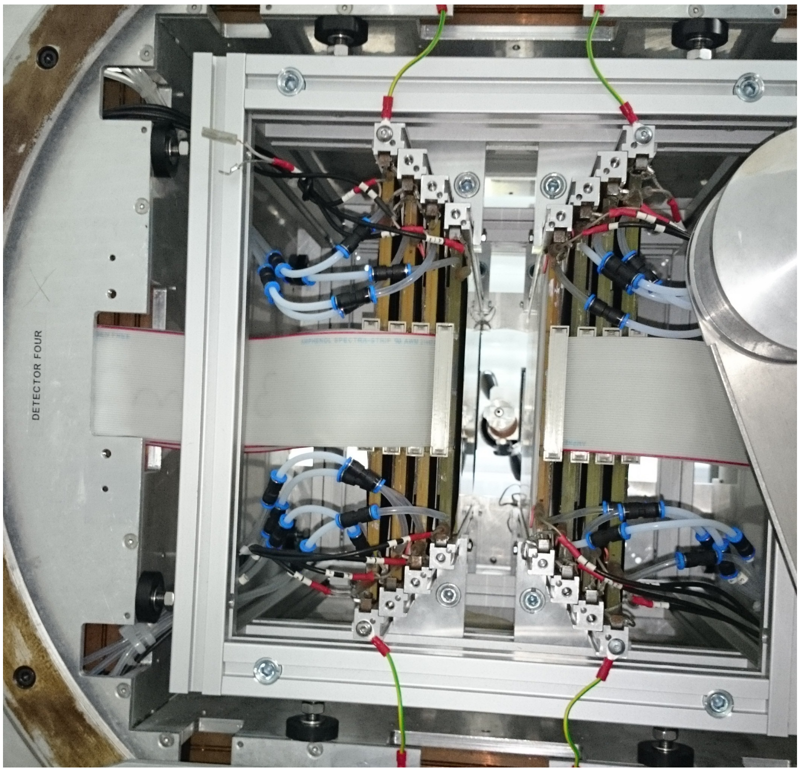

Figure 3.4: HIDAC with the inlet inside. The inlet is used to carry and position the modules to certain distances.

Measurements of High Resolution HIDAC

The high resolution HIDAC has been used for different kinds of measurements. At first a spherical Na^{22} source with an activity of 1 MBq and a diameter of 250 μm was placed inside the HIDAC and the spatial activity distribution of the source was measured. This measurement took 3480 min and the rotation of the gantry was turned off. One difficulty can be seen in the parallel projections. A parallel projection in PET is a plane considering only those coincidences perpendicular to that plane. Parallel projections of first measurements of the source can be seen in

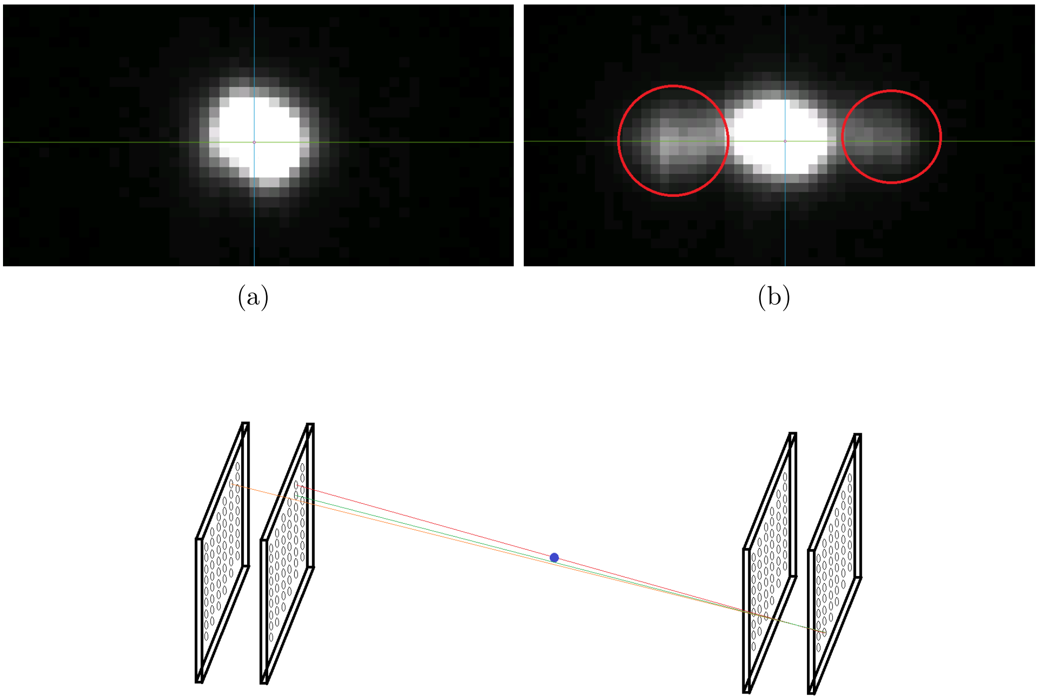
(a)

(b)

(c)

Figure 3.5: (a)(b) Parallel projections performed by the high resolution HIDAC with a Na^{22} source of a diameter of 250 μm and an activity of 1 MBq. A pixel in the parallel projections equal a distance of 0.2 mm. (a) Parallel projection with coincidences orthogonal to the modules (small angle)(b) Parallel projection with angles more oblique to the modules; The red marked area shows artifacts that occur when looking at oblique angles. These artifacts result in decreased resolution in reconstructed images (c) Illustration of the deviation given by interpreting the event at a wrong converter plane or hole

3.5. The artifacts shown in 3.5(b) are the result of improper interpretation of events. If the readout interprets an event as created at the wrong hole position or even a wrong converter, the deviation of the estimated source position given by the LOR differs more for oblique angles. A schematic illustration of this deviation can be seen in figure 3.5 (c). Due to this deviation the analysis only uses coincidences in a small solid angle which are nearly perpendicular to the modules. This reduces the statistic and therefore, increases the time of measurements needed to get comparatively good results. The degradation of the resolution by the use of oblique angles has also been reported in [10]. The National Electrical Manufacturers Association (NEMA) has published widely used resolution tests to be able to compare different PET systems. Instead of using a more complex NEMA method, in this case a simple line plot was produced through the center of the distribution in a parallel projection in x- and y-direction. By calculating the full width at half maximum (FWHM) of the distributions of the line plots, figure 3.6 has been created. As it can be seen in 3.6(b) the decrease in module distance results in an improvement of the resolution for the y-direction. However, in the x-direction, no improvement is measurable. To understand that, the hitmap of coincidences for a detector module can be considered. This hitmap is also an image of half-coincidences. Figure 3.7 (a) shows an image of half-coincidences of a detector module in a measurement with the described Na^{22} source. Projecting the half-coincidences of figure 3.7 onto the x-axis results in figure 3.7 (b). If just the distribution of the peak heights are considered, they describe the

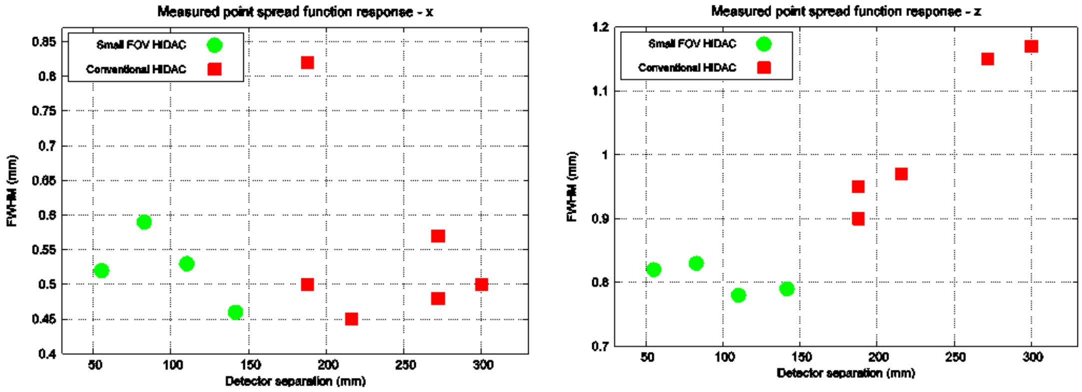

(a) (b)

Figure 3.6: Module separation against FWHM of line plot in parallel projection in (a) x-direction and (b) y-direction

expected response given by a spherical source. However, the ideal distribution would be homogeneous. The distance between the peaks is 1.5 mm, which is the distance between the wires. Therefore, the stripes seen in figure 3.7 can be interpreted as the binning of the events by the readout of the wire locations.

Hence, to get a better understanding of the binning and the resulting resolution in x-direction it is useful to measure the pad response function of a module to be able to calculate the real displacement of an event.

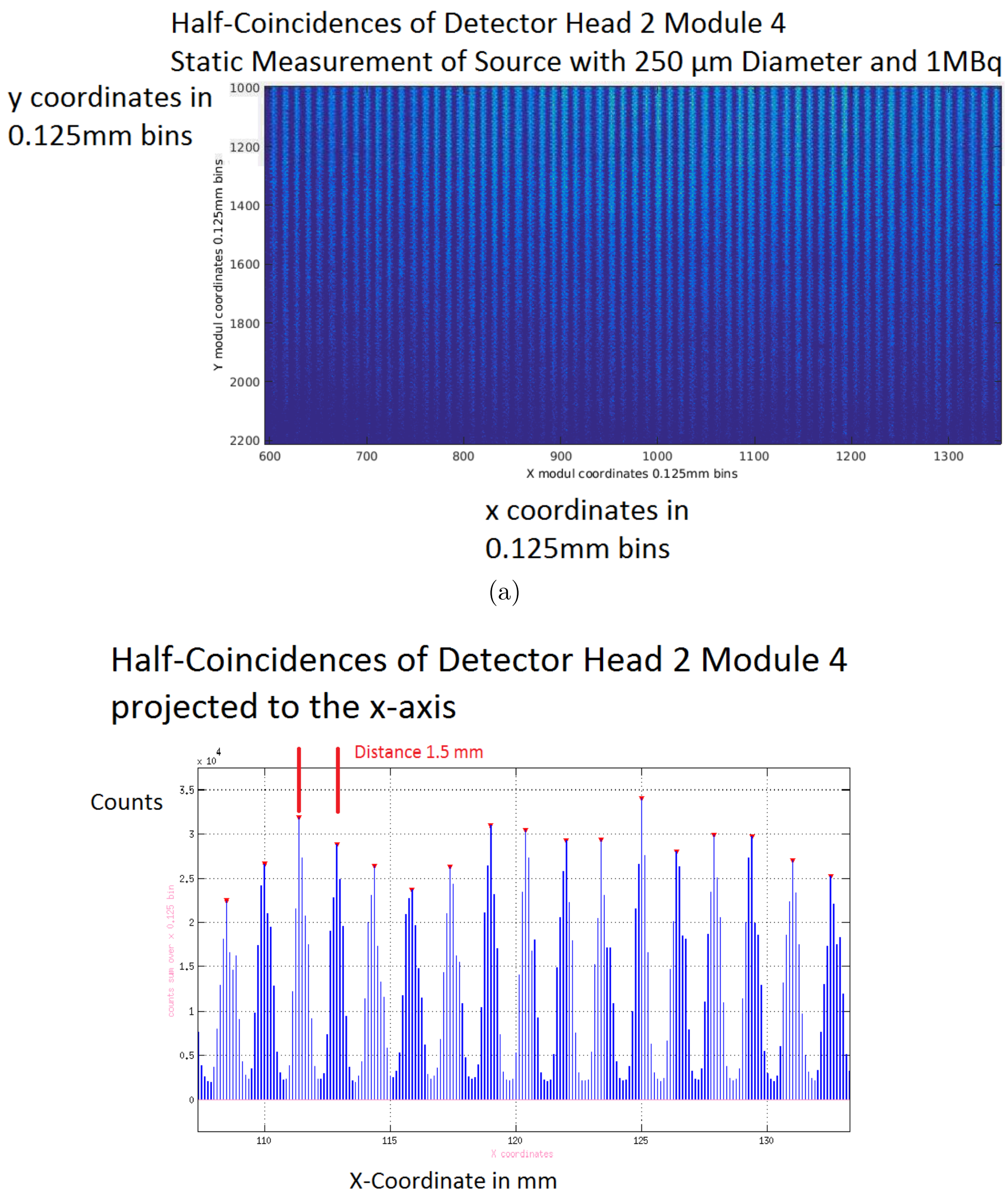

(a)

(b)

Figure 3.7: (a) Image of half-coincidences of a detector head 4 module 2 in the static measurement of 3480 min of a spherical source with 250 μm diameter and an activity of 1 MBq (b) Projection of the half-coincidences shown in (a) to x-axis

4 Determination of Displacement

As described in section 3.0.1, to achieve a better spatial resolution, it is important to gather information about the PRF and calculate the displacement of the events in the module. The way of choice to aquire the PRF in this work makes use of a scintillation dectector.

4.1 Setup with Scintillator

A photograph of the readout-setup used in this work is shown in figure 4.1(a). A HIDAC module is attached to an aluminum framework which fixes its position. The power supply used for the anode wires is called NHQ 203L, while a NHQ 204M power supply is used for the converters. The high voltage supply at the anode wire is decoupled capacitively and amplified with help of a GSI VV1001 charge sensitive preamplifier. This enables the voltage drops caused by the avalanche inside the HIDAC module during an event to be visualized on an oscilloscope. The pad signals measured at the HIDAC module are amplified by a charge sensitive PNG CATSA preamplifier. This signal is reshaped by a PNG MA8000 main amplifier. This amplifier is sensitive to the edges of an input signal. Its output signal is digitized by an Analog to Digital Converter (ADC) named CAEN V785N. This ADC has 16 channels, whose names are enumerated from 0 to 15. It is peak sensitive and needs to be triggered by an external gate. It is read out by a computer with help of a program written by Jan Pietschmann [16]. Each time a gate is triggering the ADC readout, an event is created. The voltage height of every channel in an event is converted to an integer value from 0 to 3840. Events with values above 3840 are considered as not correct and will not be analyzed. The data and written to a csv file, where every row stores an event and every column refers to a channel. A Harshaw Integral line scintillation crystal of type S6/2E made of NaI (TI) with a diameter of 1.5 cm and an attached scintillator is used as photon detector. Its power supply is realized by a Harshaw NV-25A. The signal of the scintillator is splitted into two parts. One

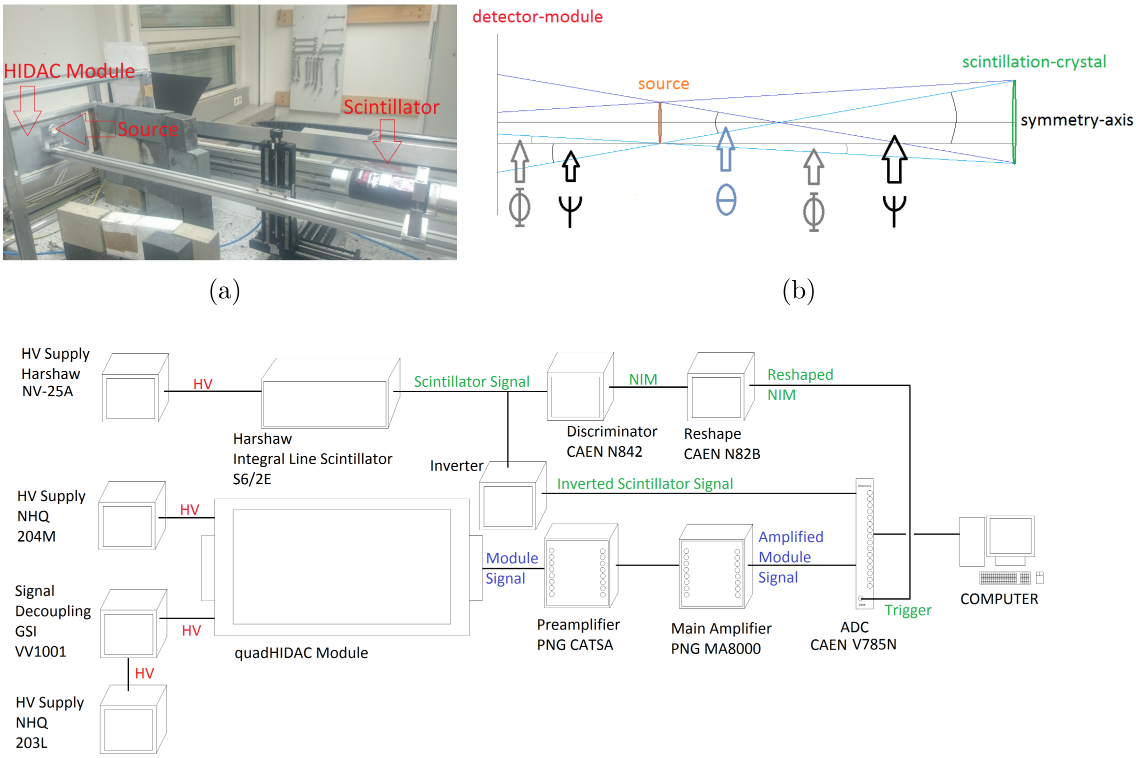

(a) (b)

(c)

Figure 4.1: (a) shows a photograph of the readout setup while (b) shows the principle of the readout. A β^+-source emits a positron which annihilates with a nearby electron and two photons are emitted with an angle of approximately 180°. The photons are detected by the module and the photon detector and therefore, create a coincidence which defines the sensitive detector distance (y-direction) (c) Electronic readout setup with scintillator used in this work

part is inverted and used as input signal for a CAEN N842 discriminator. If the input signal (trigger signal) is greater than a given threshold value, the discriminator creates a Nuclear Instrumentation Module (NIM) pulse (negative rectangular pulse of approximately $-0.8\,\mathrm{V}$ and $300\,\mathrm{ns}$) as output signal. This NIM-pulse is reshaped in length by a CAEN N93B to be in accordance with the measured signals and is used as a gate for the ADCs. The second part of the scintillator signal is coupled into an ADC channel and read out during the measurements. The used gas inside the HIDAC module is a mixture of argon with CO_2 as quenching gas. It has been shown by [17] that a good working gas ratio is 10 : 1. Recent experience has shown that a ratio of 9 : 1 is also a viable gas mixture. In this work, the gas flow is set to 90 sccm (Standard Cubic Centimeters per Minute) for argon and 10 sccm for CO_2. Between the HIDAC module and the photo detector, a spherical Na^{22}-source with a diameter of 250 μm and an activity of approximately 200 kBq is placed. The source and the scintillation crystal are attached to an aluminum bar with a total length of 1.5 m. As a β^+-emitter, Na^{22} emits a positron which annihilates with a nearby electron as discussed in section 2.1. The two created photons, emitted under an angle of approximately 180°, have the possibility to be either detected by none, one or both detectors (photon detector and module). The photon detector and the HIDAC module enable two tasks: By verifying that the event measured at the HIDAC module is also measured at the photon detector, the event can be classified as true event. Furthermore, due to the geometry shown in 4.1(b) and (c) the sensitive area of the detector system can be modified. The aluminum arm holding the source and the scintillator is able to move in three directions. This way by adjusting the position of the arm different the sensitive areas are set. The sensitive area on the detector module caused by the coincidence setup is a circle with diameter d_{mod}. As this work only focuses on the y-direction, the diameter is now called sensitive detector distance. The diameter of the source is called d_{sour}, the diameter of the scintillation crystal is called d_{scin}, the distance from source to module is called $l_{\text{mod-sour}}$ and the distance from the scintillation crystal to the source is called $l_{\text{scin-sour}}$. Figure 4.1 (c) shows a schematic image of the sensitive detector distance in the y-direction. The black line shows a symmetry line. It is approximated that the scintillator, the source and the detector module are centered on this symmetry line. For the drawn angles, the following geometric correlations can be seen:

$$\tan(\Phi) = \frac{d_{\text{scin}}/2 + d_{\text{sour}}/2}{l_{\text{scin-sour}}} \tag{4.1}$$

$$\tan(\Psi) = \frac{d_{\text{scin}}/2 - d_{\text{sour}}/2}{l_{\text{scin-sour}}} = \frac{d_{\text{mod}}/2 - d_{\text{sour}}/2}{l_{\text{mod-sour}}} \tag{4.2}$$

$$\begin{aligned} \Rightarrow d_{\text{mod}} &= \left(\frac{d_{\text{scin}}/2 - d_{\text{sour}}/2}{l_{\text{scin-sour}}} \cdot l_{\text{mod-sour}} + d_{\text{sour}}/2 \right) \cdot 2 \\ &= \frac{d_{\text{scin}} - d_{\text{sour}}}{l_{\text{scin-sour}}} \cdot l_{\text{mod-sour}} + d_{\text{sour}} \end{aligned} \tag{4.3}$$

with

$$\Delta d_{\text{mod}} = [(\frac{d_{\text{scin}} - d_{\text{sour}}}{l_{\text{scin-sour}}}\Delta l_{\text{mod-sour}})^2 + (\frac{\Delta d_{\text{scin}}}{l_{\text{scin-sour}}} l_{\text{mod-sour}})^2 \tag{4.4}$$

$$+ (\frac{d_{\text{scin}} - d_{\text{sour}}}{l^2_{\text{scin-sour}}} l_{\text{mod-sour}} \Delta l_{\text{scin-sour}})^2 + (\frac{-\Delta d_{\text{sour}}}{l_{\text{scin-sour}}} l_{\text{mod-sour}} + \Delta d_{\text{sour}})^2]^{\frac{1}{2}} \tag{4.5}$$

The used source has a diameter of 0.25 mm while the diameter of the scintillator has a diameter of 15 mm. The errors of these diameters are considered as negligible. Hence the calculated error is dependent on the error of the distances of the module and the scintillator to the source.

$$\Rightarrow \Delta d_{\text{mod}} = [(\frac{d_{\text{scin}} - d_{\text{sour}}}{l_{\text{scin-sour}}}\Delta l_{\text{mod-sour}})^2 \tag{4.6}$$

$$+ (\frac{d_{\text{scin}} - d_{\text{sour}}}{l^2_{\text{scin-sour}}} l_{\text{mod-sour}} \Delta l_{\text{scin-sour}})^2] \tag{4.7}$$

Every HIDAC module has a data plug for the x-direction and the y-direction. Each data plug has two sides with 25 contacts (connections) each. One side is completely grounded and one side is used for the data readout. Only the data side will be discussed. As described in chapter 3, the modules have a different number of cathode tracks in x-direction depending on their size. As the y-direction has the same number of cathode tracks for every module, each module has the same plug assignment in this direction, whereas the x-direction has a changed plug assignment depending on its size. The first 12 connections of a plug are referring to the groups. The missing cathode tracks reduce the number of groups a module has. Depending on how many tracks are missing, the first to the i^{th} group are missing and the referring connection is grounded. If the number of missing tracks does not equal 24, which is the number of maximal tracks in a group, the group is implemented with a reduced amount of tracks. The 13th connection is grounded and the 14th to the 25th connection are referring to the blocks of the module. To be able to calculate the localization of an event the 14th to the 25th connection are used in every module. Therefore these groups are never grounded. Due to this principle, there can be a different amount of tracks inside one block. To reduce the amount of channels to be read out in this work, only the three central groups, but all blocks are read out. Hence including the channel for the photon detector 16 channels are read out.

4.2 Validation and Calibration of Setup

To acquire significant results it is inevitable to calibrate the used channels. In a first iteration, the same pulse was used as an input signal for all channels. The output signal was monitored on an oscilloscope. By changing the gain of the main amplifier channels an output pulse of approximately the same voltage height was achieved. The second iteration makes use of input signals with different heights. Rectangular pulse signals are created by an external pulse generator called Tektronix AFG 3021. The amplifier chain (i.e. preamplifier followed by main amplifier) responds to the edges of the rectangular pulse. It then creates a negative pulse followed by a positive pulse as shown by the yellow signal depicted in figure 4.2. The pulse generator is only able to create signals of a minimal pulse height of 10 mV. This quickly results in signals too high for the preamplifier. Therefore, the signal heights are reduced with the help of an attenuator of 13 dB. To be able to trigger on the created pulse the signal is split into two parts. While the ADC needs a signal of positive voltage, the discriminator needs negative signals. Due to this, one part of the signal is inverted and used as input signal for the discriminator to create a gate. This gate is reshaped in time length by the CAEN N93B module. The second part of the

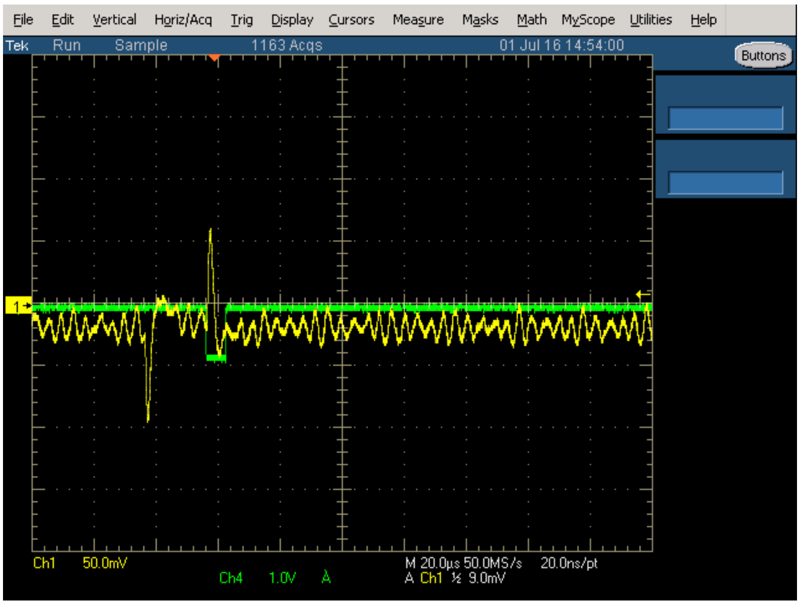

Figure 4.2: The yellow signal is created by an external rectangular pulse which undergoes the amplification chain. The edges of the external pulse are shaped to the negative and positive pulse. The gate (green) defines the time window for the ADC to read out the signal.

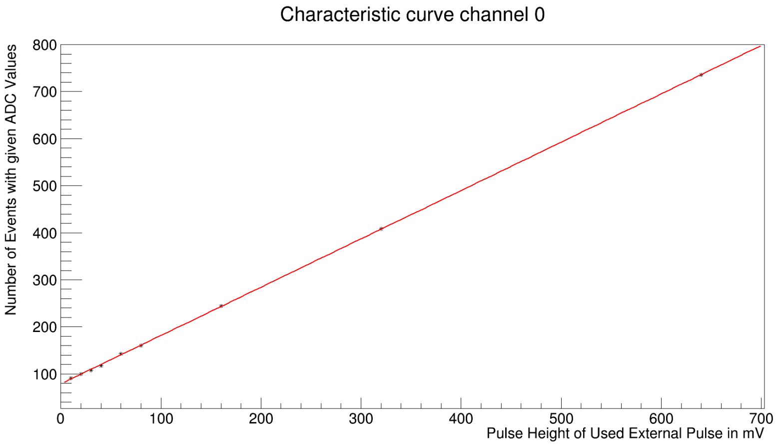

Figure 4.3: Characteristic curves of channel 0. The y-intercept gives a baseline value, whereas the slope is used to calculate the amplification factor for the channel.

pulse is used as input for the amplifier chain and digitized by the ADC. The green line in figure 4.2 shows the created gate. The different pulse heights enables the analysis software to calculate a value for the baseline and amplification for every channel. For every pulse height, multiple events are measured and the average value is calculated. These average values are then drawn against the voltage values of the used external pulses. Fitting these values results in characteristic curves for each channel (figure 4.3). The y-intercept is used as a value for the baseline subtraction. The slopes are used to calculate the amplification factor of each channel. To achieve this an average value for the slopes is created. The average value is then divided by the slope values of the different channels. The gained amplification factor can be multiplied to the measured ADC values. During this work, multiple preamplifier channels broke and were changed, so the baseline and the amplifier correction factor can differ in measurements.

To validate the scintillator its signal needs to be split into two parts. The scintillator creates signals positive of voltage. One part of the split signal is coupled directly into an ADC channel. The needed gate is created with the help of the second part of the split signal. It is inverted and used as input for the discriminator. In this way, the spectrum of the ^{22}Na source can be measured. Multiple measurements with different discriminator threshold values were carryed out. The result of two measurements can be seen in figure 4.4. The first peak in figure 4.4(a) shows the scintillator spectrum for a discriminator threshold value of $-3\,\mathrm{mV}$. The region up to

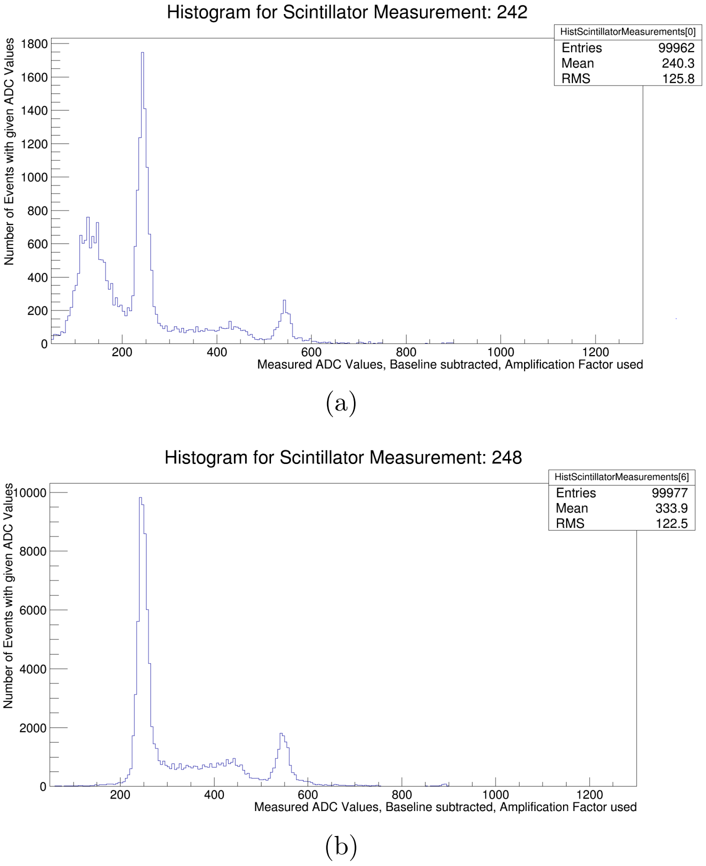

Measurement Number	Used Discriminator Threshold in mV
242	-3
248	-9

Figure 4.4: (a),(b) Spectrum of the used ^{22}Na source measured with help of a scintillator and different thresholds at the discriminator. The 511 keV peak can be identified between an ADC value of 200 and 300. (c) Used thresholds of discriminator for the measurements shown in (a) and (b).

ADC values of 200 is identified as the Compton background, while the 511 keV peak lies between an ADC value of 200 and 300. When increasing the threshold value, low ADC values are cut away. Figure 4.4(b) shows the scintillator spectrum using a threshold value of -9 mV. The Compton background is cut away and only photons of 511 keV, within the apparent resolution, or higher energies are used. The peak at an ADC value between 500 and 600 can be identified as the 1275 keV peak of the deexcitation of the ^{22}Ne, that is created during the β-decay of ^{22}Na.
To validate the behavior of the module an external signal is coupled into the pads and the response function of the anode wires is measured with help of the GSI VV1001. The result can be seen in figure 4.5. The purple signal shows the injected external pulse, whereas the green curve shows the decoupled signal of the anode wire.

The length of the input signal is limited by the external pulse generator and has an approximated duration of 300 ns, while the anode response has a approximated duration of 600 ns. This shows that the time resolution of the decoupled anode signal is 600 ns or shorter.

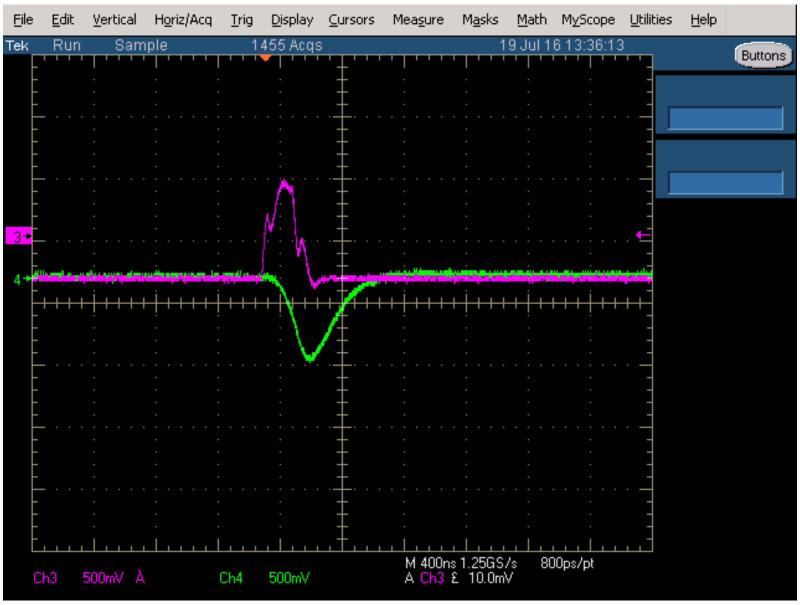

Figure 4.5: The purple curve shows the input signal which is coupled into the module pads. The green curve shows the response of the anode wires.

When applying a converter voltage of −2700 V and an anode voltage of +1900 V the module is in area of operation. Figure 4.6 shows the measured signal of a single event. The green curve shows a gate of 20 μs, triggered by the scintillator. The blue curve shows the measured anode wire signal, the purple curve shows the signal of a pad group after the preamplifier and the yellow curve shows the same signal after the main amplifier. The yellow signal is used as input for an ADC channel, while the green gate defines the time window for an event. The pad signal, induced by the absorption of the electrons at the wire, is represented by the first positive peak of the yellow curve.

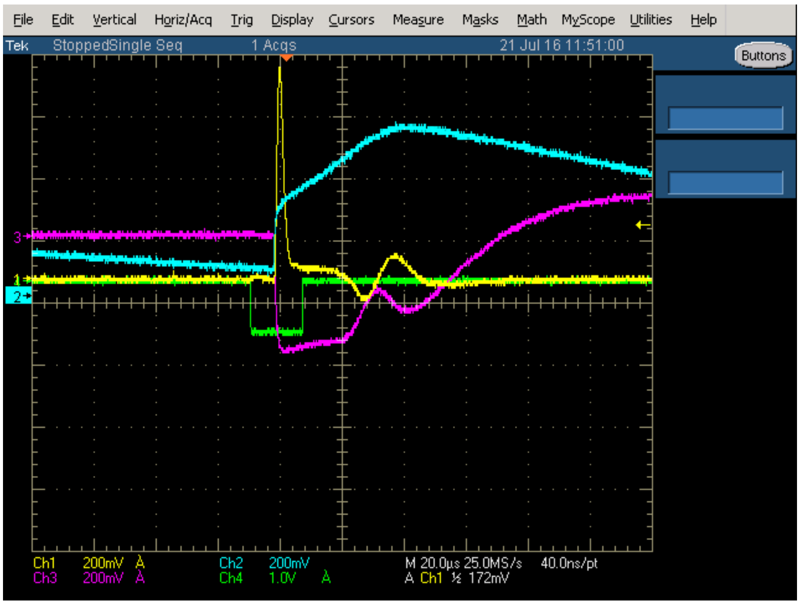

Figure 4.6: Measured pad signal of an event after the preamplifier (purple), after the mainamplifier (yellow) and the corresponding anode signal (blue). The green curve show the gate triggered by the scintillator.

4.3 Measurements and Analysis

4.3.1 Analysis Code

As described in section 4.1, the acquired data is stored into a csv file. Every row has 16 integer values which represent the maximal voltage values of the 16 ADC channels measured during an event. For the pad channels these voltages refer to the deposited charges on the pads. As shown in section 4.2, the software calculates a baseline and an amplification correction factor for every channel. Every ADC value receives a baseline subtraction and gets multiplied by its amplification correction factor. In the next iteration, the code distinguishes between channels with block, group or scintillator information. A channel with the maximum value is determined for the block and the group channels, while the summed charge information of all block channels is calculated. By comparing these values with threshold values, that still have to be defined, the events can be accepted as true events. Furthermore, the values gained from the scintillator channel give the possibility to make an energy cut around the region of 511 keV. Only true events are used in the further analysis. If an event is considered true, the maximum ADC values of the block channeland the values of the channels of its neighboring blocks are used to calculate the unweighted and weighted displacement function, described in 2.4.2. The pads of the blocks have a distance from center to center of 2 mm. Therefore, by defining the position of the first block channel to 0 mm a spatial distribution of the created events can be provided.

4.3.2 Measurement with a gate of $20\,\mu$s

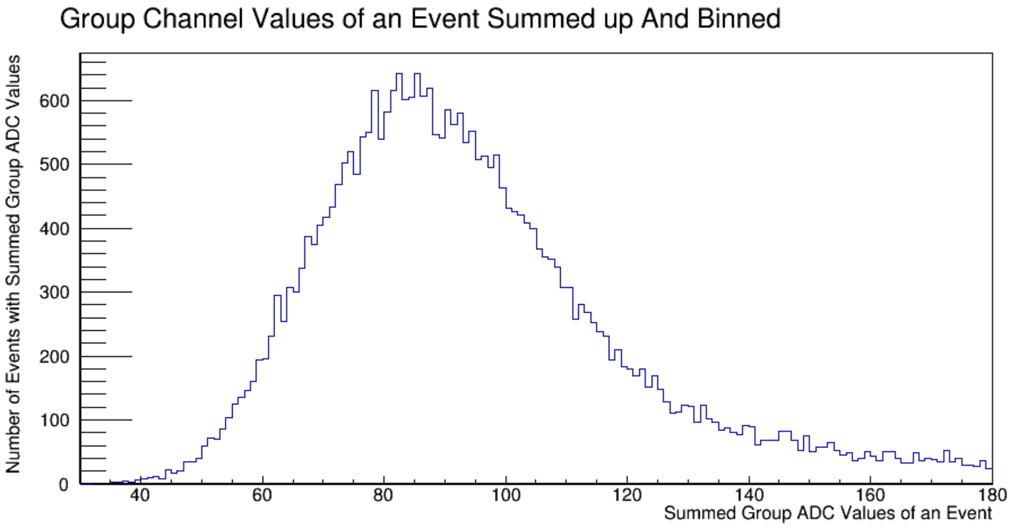

Figure 4.7: Number of events with summed up group channel values for a $20\,\mu$s gate and bottom position measurement

As discussed in section 4.2 the first yellow peak in figure 4.6 represents the induced charge on the pads during an event. This peak needs to be included by the gate, triggered with help of the scintillator. Therefore, in this series of measurements the time length of the gate was set to $20\,\mu$s. The source was placed in a distance of (20 ± 10) mm of the module, while the distance of the scintillator to the module was set to (800 ± 50) mm. This results in a sensitive detector distance of (0.4 ± 0.2) mm. The y-position of the source was increased by $300\,\mu$m from measurement to measurement. By calculating the weighted displacement function with equation 2.77 for true events, a spatial distribution for the position of the occurred events can be calculated. Changing the threshold values in the analysis code, a different amount of events are considered as true. However, no matter which threshold parameters were used, a variation of the source position could not be observed.

To verify the setup the module groups were measured. Three separate measurements with 35000 events at different source positions relative to the y-position of the HIDAC module were taken: top, middle and bottom. The converter was set to −2700 V, while the anode wires were set to 1900 V. After the subtraction of the baseline and multiplication with the amplification correction factor, the sums of the ADC values of all group channels was calculated. The distribution of this sum over all events for the measurement at the bottom position can be seen in figure 4.7. Only a small part (about 1%) of the events triggered by the scintillator create an avalanche inside the HIDAC module. The peak between a summed group value of 40 and 120 is referring to the amount of events that did not create an avalanche. Therefore, the threshold to consider an event as true was set to 150. For every event, the maximum channel was stored in a histogram. Figure 4.8 shows these

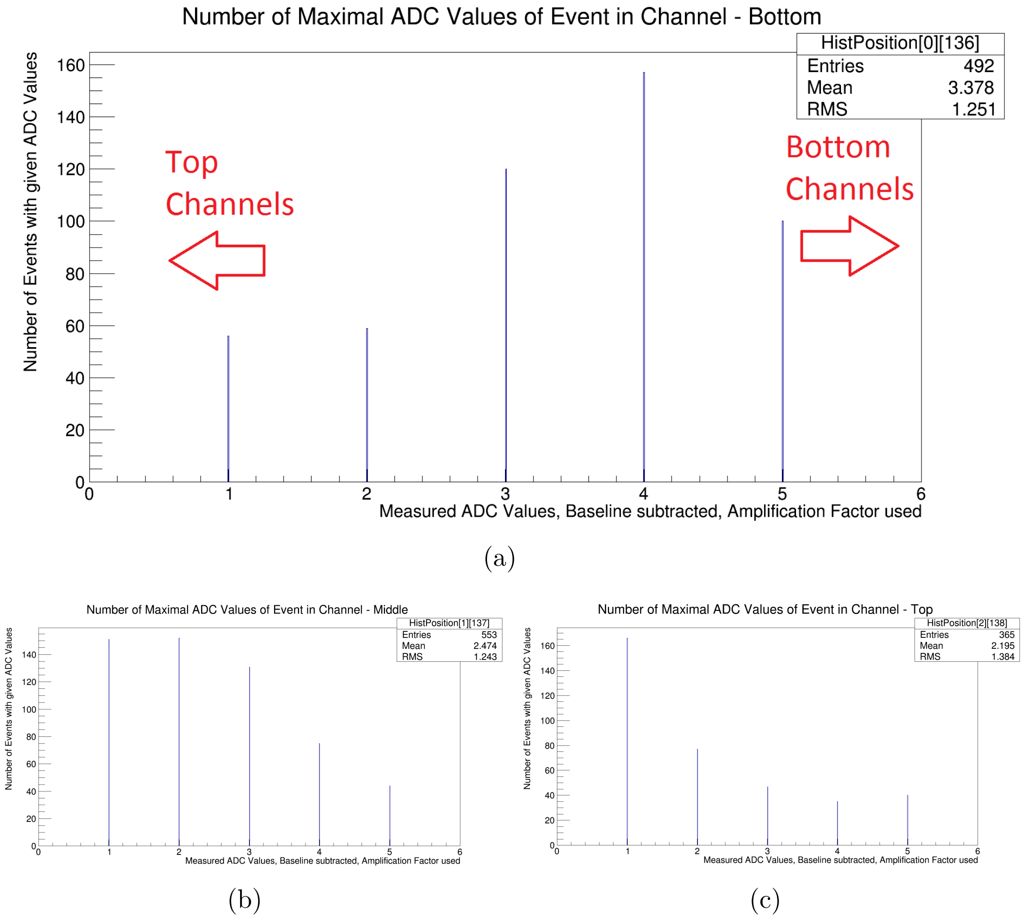

(a)

(b)

(c)

Figure 4.8: Number of maximum ADC values for each channel (a) Source position at the bottom area of the module, (b) Source position at the middle area of the module (c) Source position at the top area of the module

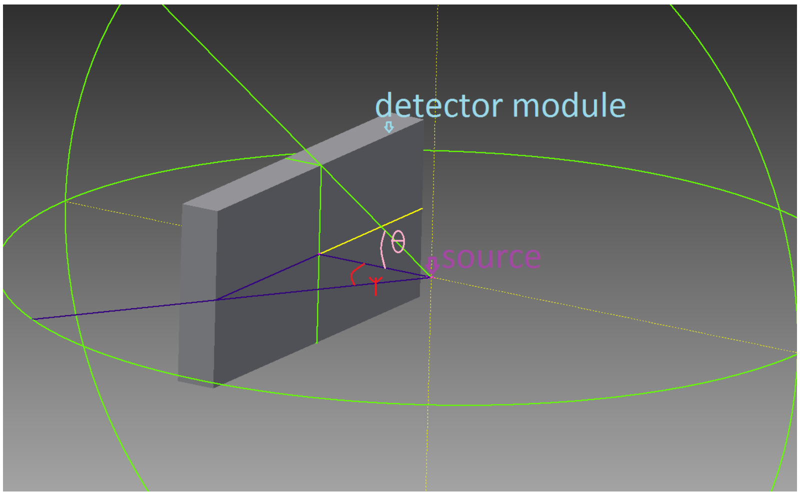

Figure 4.9: Module and the angles which define area of the module.

histograms for the three mentioned measurements. It can be seen that the mean of the distributions is shifted. However, as the groups have a distance of 24 mm from each other, it is not expected that more than one or two group channels are giving the highest ADC values during the measurements.

As it has been shown in equation 4.3, the solid angle θ for a point source in a two dimensional image can be calculated with

$$\tan(\theta) = \frac{d_{\text{mod}}/2}{l_{\text{mod-sour}}} \tag{4.8}$$

Where d_{mod} is the size of the module and $l_{\text{mod-sour}}$ is the distance between the module and the source. In three dimensions the module needs to be projected onto a spherical surface. Figure 4.9 shows the module within a sphere with the two angles θ and Ψ. For the amount of photons that hit the detector only the solid angle and the activity of the source are of relevance. This portion can be calculated by calculating the quotient q_{solid} of the detector surface and the total solid angle (4π)

$$q_{\text{solid}} = \frac{2\theta}{\pi} \cdot \frac{2\Psi}{2\pi} \tag{4.9}$$

The size of the modules is 13.5 cm × 28 cm. In the case of a distance from the module to the source of 2 cm the quotient is derived as 0.37. The source has an approximate activity of 200 kBq. Therefore, it is expected that, on average, every 6.73 μs the detector module is hit by a photon. The gate length is 20 μs, which results in an average 2.97 photons during this gate. Hence, it is not expected that single events can be resolved, so that the setup has been changed.

4.3.3 Measurement with a gate of $2\,\mu$s

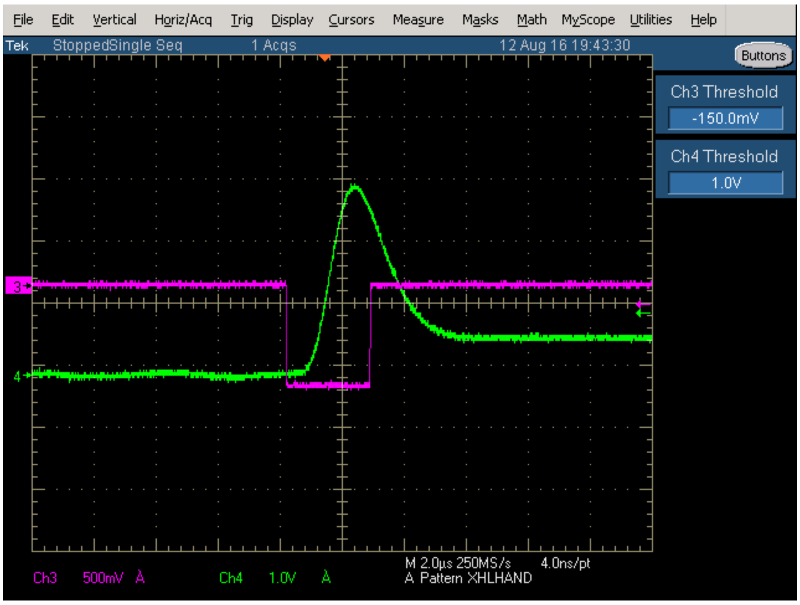

Ch3 Threshold -150.0mV

Ch4 Threshold 1.0V

Figure 4.10: First peak of pad signal (green) in coincidence with the scintillator signal, which triggers a $2\,\mu$s gate (purple)

To reduce the amount of photons during a triggered gate the length of the gate was reduced to $2\,\mu$s. Figure 4.10 shows a pad signal in coincidence with the scintillator. As the ADC is peak sensitive, only the maximum of the peak needs to be inside the gate. This prevents using gate of considerably lower length. In the measurements in this section the distance of the source to the module was (10 ± 2) mm, while its y-position was set to the center of the module. This results in a sensitive detector distance of $(0.65 \pm 0.14\,)$mm The scintillator to module distance was set to (240 ± 10) mm. ADC channel 0 to 11 were used for the block information, whereas channel 12 to 14 were used to read out the three central groups of the module. The last channel (15) carried the information of the scintillator. Between multiple measurements the source was moved step wise by $333\,\mu$m alongside the y-axis of the module. The measurements are titled by numbers shown in table 4.1 The voltage was -2750 V at the converter and 1910 V at the anode wire. The discriminator threshold was set to -9 mV. Thereby, only photons of 511 keV or harder were con-

Table 4.1: Measurement numbers and their corresponding source position

Measurement	Source Moved Relative to Zero Position in μm
254	0
270	333
272	666
256	1000
274	1333
276	1666
258	2000

sidered. Every measurement contains an amount of 600000 events. As described in section 4.3.2, the group and block values of an event can be summed up. The results of the binned histograms of the first measurement (zero position; source not moved) are shown in figure 4.11. According to the distribution, thresholds for true events were set. The summed group threshold was set to 100, while the summed block threshold was set to 300.

In the next step, the relevant groups of the source position were elaborated. To do this the values of all true events are summed up for every channel. Figure 4.12 shows the distribution of these sums for the measurements. It can be seen that for all measurements the relevant group channel is 13. Hence, as an additional condition, a true event needed to have its group maximum in channel 13. Looking at the distributions of channel 0 to 11 a shift of the maximum can already be seen. With the described thresholds and conditions, the amount of true events is defined. This way, it is now possible to calculate the unweighted and weighted displacements for every true event. With help of these displacement a spatial distribution can be calculated. The principle the analysis code uses for this measurement is diagrammed in 4.13. The spatial distribution calculated with help of the unweighted displacement can be seen in figure 4.14(a), while the spatial distribution with help of the weighted displacement is shown in figure 4.14(b). The average number of true events during these measurements is 17839 events. To evaluate number of randoms a measurement has been taken, while the triggered gate was delayed by 10 μs. When the same conditions for a true event are used, the number of trues in this measurements is 13166 events. Hence, approximately 73% of the true events can still be considered as

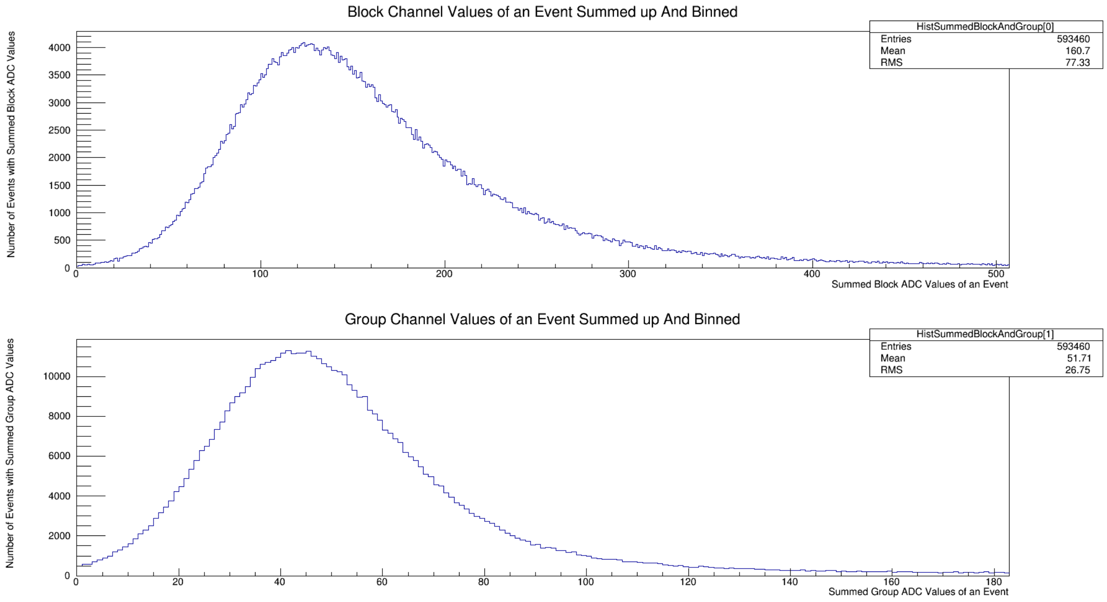

Figure 4.11: Number of events with summed up channels for blocks and groups for 2 μs gate; Measurement with y-position of source position zero; x-axis: Summed block/group ADC values of an event; y-axis: number of events with summed block/group ADC values

randoms, when using these conditions to determine the amount. This leads to a high background in the spatial distributions. The total shift of the source has been 2 mm. The calculated spatial distributions clearly shows a shift of the regions with a high amount of events. As it can be seen, the pads responding are between a position of 13 mm and 20 mm. Gaussian fits were used in these regions, whereas the position of the center of these functions defines the location of the source. This position shifts from measurement to measurement. The location of the center of the first Gaussian distribution is set to 0, as it defines the reference position of the source. By drawing the real position against the measured position the diagrams shown in figure 4.15 were elaborated. The red function shows the real positioning of the source, while the dots are showing its calculated position. The green function equals the red one, but has a reduced y-intercept of 0.7 mm. Even though the expected linear shift can be observed, the difference between the real and calculated position of the source is large. Measurements 254 (first position), 256 (fourth position) and 258 (seventh position) were taken on another day as measurements 270 (second position), 272 (third position), 274 (fifth position) and 276 (sixth position). While measurement 254 to 258 are rather close to the real source position relative to measurement

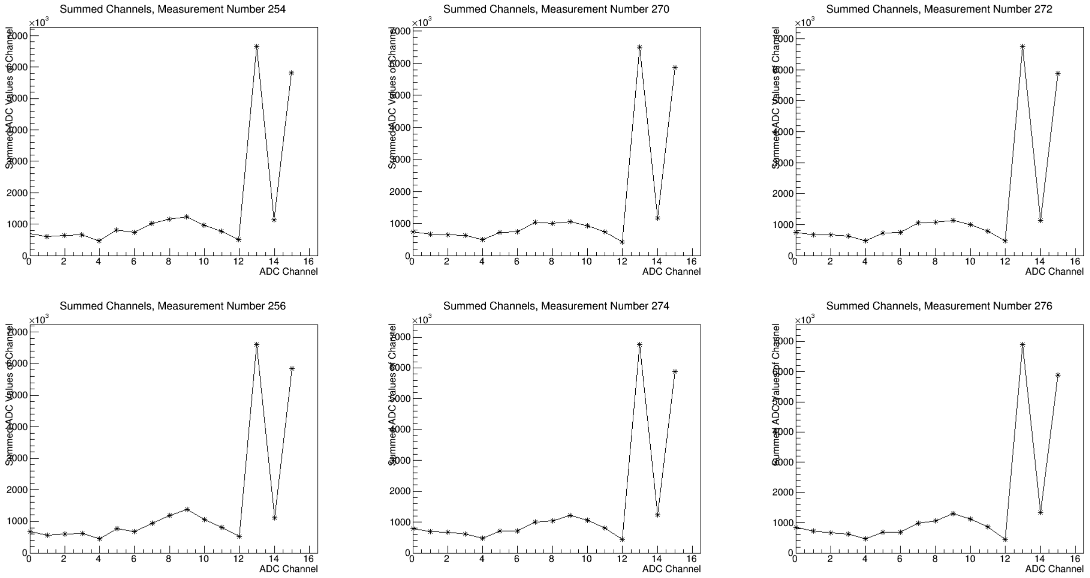
Summed Channels, Measurement Number 254

Summed Channels, Measurement Number 270

Summed Channels, Measurement Number 272

Summed Channels, Measurement Number 256

Summed Channels, Measurement Number 274

Summed Channels, Measurement Number 276

Figure 4.12: Channel values summed up for all true events; x-axis: ADC channel; y-axis: Summed ADC Values for channels

254, the position calculation of measurements 270 to 276 is shifted. Obviously, the module response can differ on a daily basis.

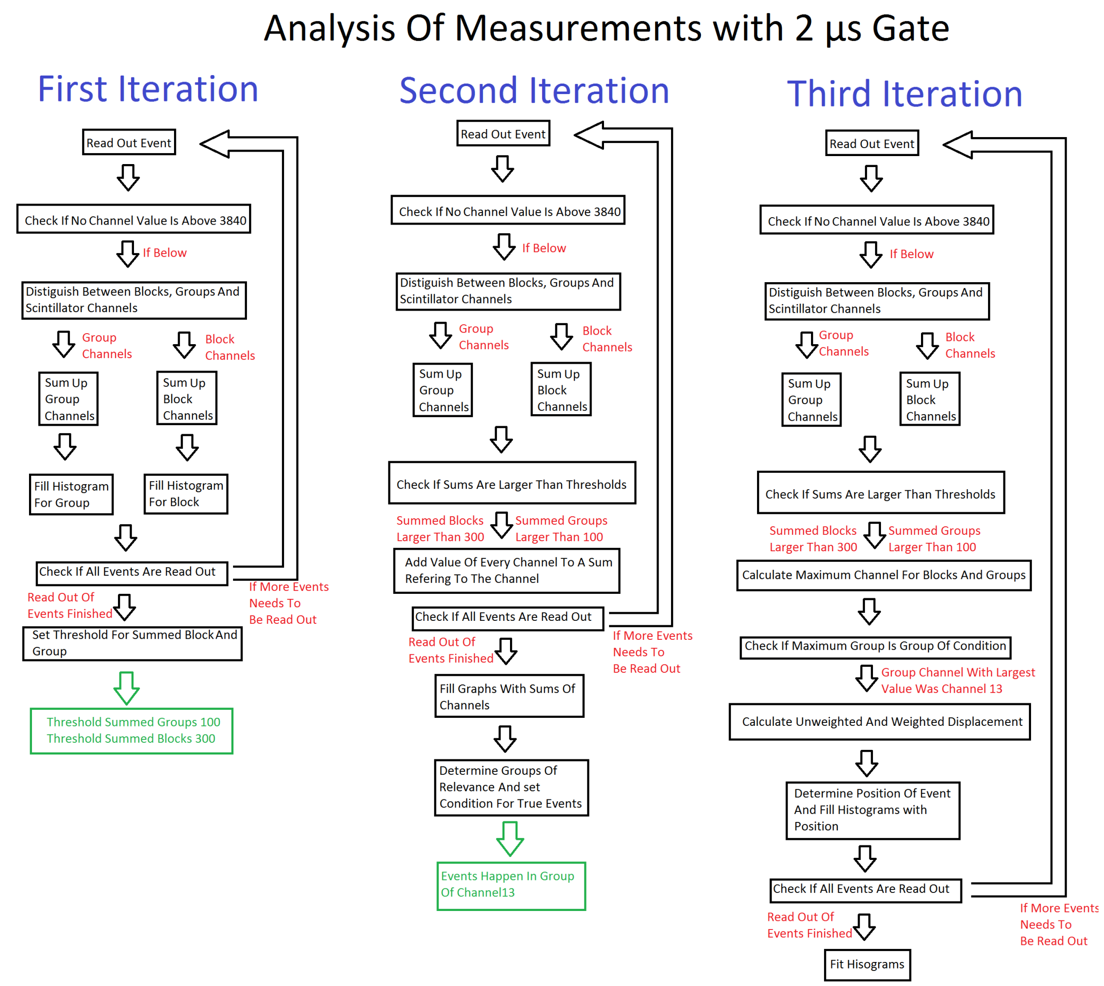

Figure 4.13: Procedure of the analysis code on the example of the $2\,\mu$s gate measurements

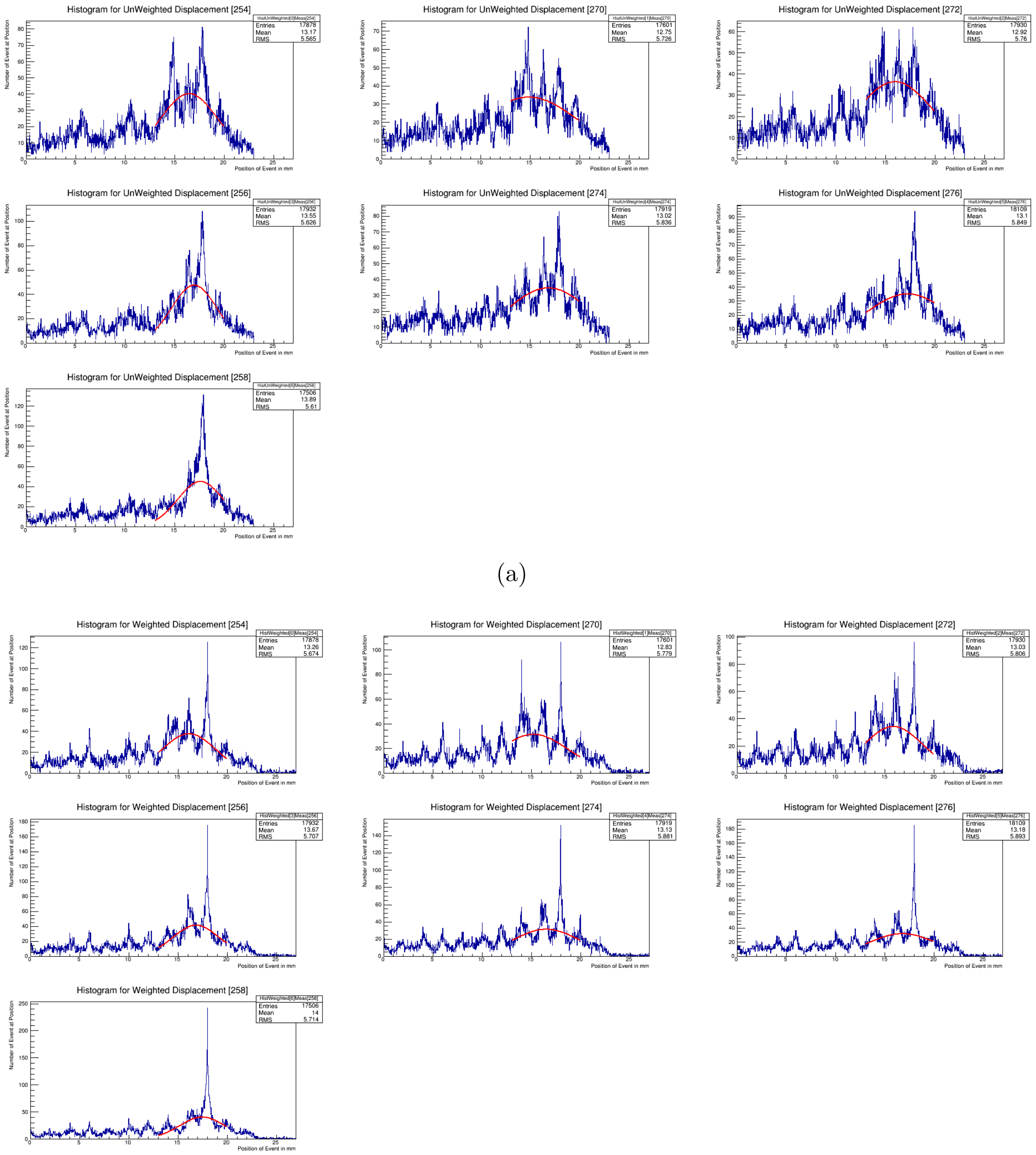

(a)

(b)

Figure 4.14: Spatial distribution calculated with help of the (a) unweighted and (b) weighted displacements. The drawn red functions are Gaussian fits in the region of 13 mm to 20 mm; x-axis: Position of event in mm; y-Axis: Number of event position

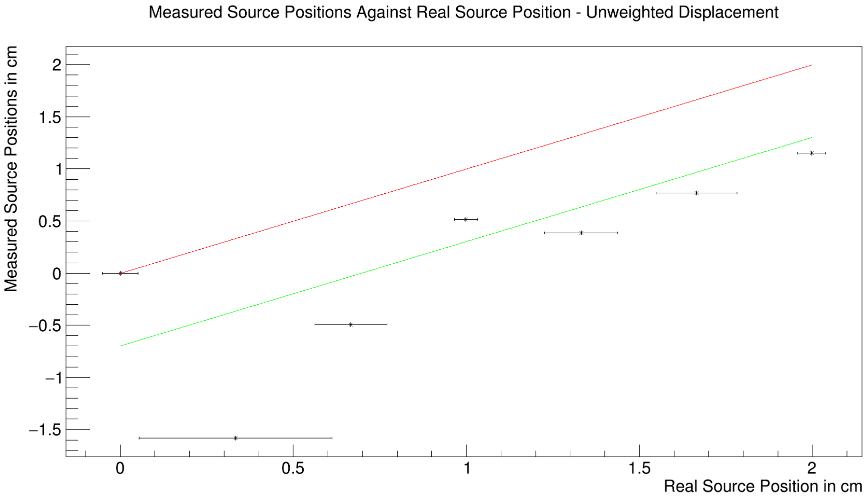

(a)

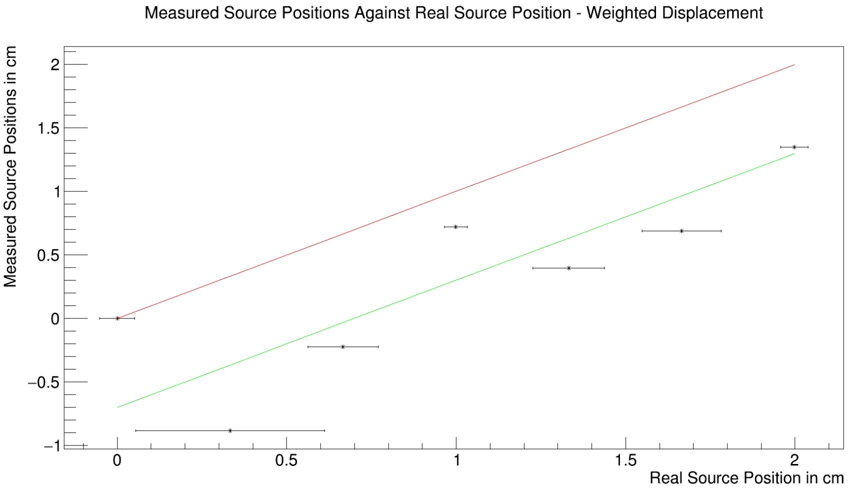

(b)

Figure 4.15: Real source positions relative to the first measurement against measured source position. (a) weighted displacement (b) unweighted displacement; The red function shows the real displacement, while the green function has a reduced y-intercept of 0.7 mm. The uncertainties are given by the fitting procedure.

5 Conclusion

This work has shown that the setup with help of a scintillator is able to elaborate the spatial distribution of the events detected in the HIDAC modules. A typical signal is exemplified in figure 4.6. The desired charge signal is represented by the first yellow peak. If the gate length is adjusted in a way that the whole signal of interest is covered, the gate becomes too long: Multiple photons of the source are expected to hit the module during this time interval. This leads to an ambiguous measurement and prevents the correct localization of the event. By shortening the gate length to $2\,\mu$s this problem could be solved. With help of the calculated displacements the changes in the source position could be observed. Moving the source in sufficiently small steps alongside the module and adding up the spatial distributions of the areas of interest (to reduce noise), a homogeneous illumination can be approximated. The emerging spatial distribution is a convolution of the spatial illumination with the transfer function of the module and the electronics. A homogeneous illumination can be characterized by a rectangular distribution. By deconvolution of the acquired spatial distributions it is possible to receive this transfer function. However, external circumstances, for example the room temperature or humidity, can lead to slightly different module responses on a daily basis.

List of Figures

Bibliography

[1] Phelps, Michael: *PET - Physics, Instrumentation, and Scanners.* Springer, 2006

[2] KP, Schäfers ; K, Bolwin ; F, Büther ; S, Hermann ; AH, Jacobs ; Kösters ; M, Kuhlmann ; M, Schäfers ; T., Viel: *Small Animal Imaging. In: Comprehensive Biomedical Physics.* Elsevier, 2014

[3] Povh, Bogdan ; Rith, Klaus ; Scholz, Christoph ; Zetsche, Frank ; Rodejohann, Werner: *Teilchen und Kerne.* Springer, 2013

[4] Grupen, Claus: *Teilchendetektoren.* Wissenschaftsverlag, 1993

[5] Kleinknecht, Konrad: *Detektoren für Teilchenstrahlung.* Teubner, 2005

[6] Lange, Wulfhard: *Einführung in die Laserphysik.* Wissenschaftliche Buchgesellschaft, 1994

[7] Simons, Lennart: *Positronium In: Corpuscles and Radiation in Matter II / Korpuskeln und Strahlung in Materie II pp 139-165.* Springer, 2014

[8] Vernekohl, Don: *Small Animal Positron Emission Tomography with Gas Detectors - Simulations, Prototyping, and Quantitative Image Reconstruction.* Doktorarbeit, 2014

[9] Blum, Walter ; Riegler, Werner ; Rolandi, Luigi: *Particle Detection with Drift Chambers.* Springer, 2008

[10] Jeavons, A.P. ; Chandler, R.A. ; Dettmar, C.A.R.: A 3D HIDAC-PET Camera with Sub-millimetre Resolution for Imaging Small Animals. (1999)

[11] E. Gatti et al.: Optimum geometry for strip cathodes or grids in MWPC for avalanche localization along the anode wires. (1979)

[12] Mathieson, E. ; Gordon, J.S.: Instr. Meth. Phys. Res. A 227, 267–276 (1984) [MAT 84b] E. Mathieson and J.S. Gordon, Cathode charge distributions in multiwire chambers, II. Approximate and empirical formulae. (1984)

[13] I. Endo et al.: Systematic Shifts of Evaluated Charge Centroid for the Cathode Read-Out Multiwire Proportional Chamber. (1981)

[14] *Oxford Positron Systems: Webside: http://www.didcotwebdesign.co.uk/ops/style/fullsizehidac.jpg.* 2016

[15] Bolwin, Konstantin: *Aufbau eines Teststandes zur Evaluierung von Vieldraht-Proportionalkammern einer quadHIDAC PET Kamera in Hinsicht auf Alterung und Wiederherstellung.* Diplomarbeit, 2010

[16] Pietschmann, Jan-Frederick: *Developement of a Novel Readout System for Small Animal Positron Tomography.* Diplomarbeit, 2008

[17] Bersch, Jennifer: *Development of Small Animal PET Detectors based on Multi-Wire Proportional Chambers.* Diplomarbeit, 2011